Multiscale extended finite element method (MS-XFEM)
Analysis of fractured geological formations under compression

Xu, Fanxiang; Hajibeygi, Hadi; Sluys, Lambertus J.

DOI
10.1016/j.jcp.2025.113998

Publication date
2025

Document Version
Final published version

Published in
Journal of Computational Physics

Citation (APA)
Xu, F., Hajibeygi, H., & Sluys, L. J. (2025). Multiscale extended finite element method (MS-XFEM): Analysis of fractured geological formations under compression. *Journal of Computational Physics*, *533*, Article 113998. https://doi.org/10.1016/j.jcp.2025.113998

Journal of Computational Physics 533 (2025) 113998

Contents lists available at ScienceDirect

Journal of Computational Physics

journal homepage: www.elsevier.com/locate/jcp

Multiscale extended finite element method (MS-XFEM): Analysis of fractured geological formations under compression

Fanxiang Xu [a,*], Hadi Hajibeygi [b], Lambertus J. Sluys [a]

[a] Department of Materials, Mechanics, Management and Design, Delft University of Technology, Delft, 2600GA, the Netherlands
[b] Department of Geoscience and Engineering, Delft University of Technology, Delft, 2600GA, the Netherlands

ARTICLE INFO

Keywords:
Multiscale extended finite element method
Fractured formations
Slip
Fracture propagation

ABSTRACT

The activation of fracture networks poses significant risks and raises safety concerns for projects involving such geological structures. Consequently, an accurate and efficient simulation strategy is essential for modeling highly fractured subsurface formations. While the extended finite element method (XFEM), coupled with the penalty method, effectively models slip-stick conditions along fracture surfaces and fracture propagation under compression, its efficiency declines when handling dense fracture networks. To address this challenge, a multiscale XFEM (MS-XFEM) approach is developed and presented. MS-XFEM approximates fine-scale displacement field by interpolating solutions on a coarser-scale mesh using algebraically constructed basis functions. All extra degrees of freedom (DOFs) are incorporated within the basis functions matrix, rendering the coarse-scale system a standard finite element-based system. In each propagation step, basis functions are algebraically and locally updated to capture fracture propagation. Through four proof-of-concept test cases, the accuracy and efficiency of MS-XFEM in simulating fractured geological formations are demonstrated, emphasizing its potential for real-world applications.

1. Introduction

Fractured geological formations play a pivotal role in the energy transition, particularly in hydrogen storage and carbon sequestration [1–9]. Disturbances to the equilibrium of these formations, especially during fluid injection or production, may activate fractures, leading to sliding along major faults and subsequent fracture propagation. Such events can result in adverse consequences, including induced earthquakes and leakage of injected fluids, which pose significant risks to both personnel and infrastructure. Consequently, developing accurate and efficient simulation strategies to understand deformation and fracture propagation in these formations is crucial for effectively mitigating these risks.

The extended finite element method (XFEM), widely used in fracture mechanics, offers a precise and efficient approach for simulating deformation and fracture propagation in highly fractured geological formations [10–13]. As an embedded method, XFEM eliminates the need for extensive unstructured grids and the remeshing when simulating complex fracture networks [14–28]. XFEM accomplishes this through the use of enrichment functions, which, when multiplied by shape functions, effectively represent discontinuities caused by fractures. Extra degrees of freedom (DOFs) are introduced at enriched nodes to satisfy the partition of unity (PoU) [29]. This simplification in mesh selection makes XFEM particularly advantageous for simulating highly fractured subsurface formations.

While XFEM offers an effective approach for simulating highly fractured formations, challenges persist in its application to real-world

* Corresponding author.
E-mail addresses: peterxu1994@gmail.com (F. Xu), H.Hajibeygi@tudelft.nl (H. Hajibeygi), L.J.Sluijs@tudelft.nl (L.J. Sluys).

https://doi.org/10.1016/j.jcp.2025.113998
Received 14 April 2024; Received in revised form 4 April 2025; Accepted 6 April 2025

Available online 11 April 2025

subsurface formations. The large number of fractures in fractured geological formations leads to a significant increase in the number of extra DOFs that must be computed. As a result, maintaining computational efficiency remains a major challenge when applying XFEM in geoscientific applications. To address this, homogenization or upscaling can be coupled with XFEM to enable the use of coarser grid sizes [30–37]. However, this approach often compromises accuracy and limits the ability to capture detailed deformation features, such as fracture slip, within subsurface geological formations.

The multiscale strategy is employed alongside XFEM to delicately balance efficiency and accuracy while preserving XFEM's inherent convenience [38–47]. This strategy maintains accuracy by constructing basis functions capable of capturing fine-scale heterogeneities, which are then used to establish a coarse-scale matrix system based on coarser-level meshes. Notably smaller in size compared to the original fine-scale system, this coarse matrix significantly enhances overall efficiency. The final fine-scale solution is obtained by interpolating the solutions on the sparser coarse-scale grid using these basis functions. In a fracture mechanics context, the recent development of the multiscale extended finite element method (MS-XFEM) by Xu et al. addresses the simulation of fractured materials under tensile loading [48,49]. This method incorporates fractures into the basis functions, generating a finite element–type system on the coarse-scale mesh without extra DOFs. During fracture propagation, the basis functions are updated locally and algebraically to capture the extension of these fractures. The extra DOFs do not impose an additional computational burden during the coarse-scale solution process; they merely contribute to an increased size of the basis functions.

This study extends MS-XFEM to simulate the deformation and fracture propagation of fractured formations under compression. The Kuhn-Tucker conditions are used to determine contact between fracture surfaces, while Coulomb's law of friction governs slip along the fracture surfaces [50–52]. To prevent interpenetration between fracture surfaces, the penalty method is employed, introducing artificially high stiffness to the fractured elements. This contact and stick-slip behavior is captured by the basis functions within MS-XFEM. Unlike fractures propagating under tensile loading, fracture propagation under compression occurs in a mixed-mode setting. Contact and slip behavior (mode-II) along the original fracture induce opening of the newly propagated fracture segments, may result in a localized mode-I fracture propagation process. The basis functions in MS-XFEM are constructed to capture self-contact between fracture surfaces and are locally updated to represent fracture propagation, following the same algebraic method demonstrated in [48,49]. Additionally, an iterative strategy is employed in post-processing to minimize errors when simulating intricate fracture networks.

The structure of this paper is as follows. First, the governing equations are presented in Section 2, along with formulations addressing the self-contact problem and fracture propagation. Next, in Section 3, the fine-scale strategies are detailed, employing the fine-scale extended finite element method (XFEM) coupled with the penalty method to simulate deformation and fracture propagation under compression. Following this, Section 4 elaborates on the principles governing the application of MS-XFEM, including a discussion on basis function updates. Finally, five numerical test cases are presented in Section 5 to demonstrate the accuracy and efficiency of MS-XFEM in simulating deformation and fracture propagation in underground formations.

2. Problem formulation

Consider a domain Ω with its boundary surface defined as Γ, as shown in Fig. 1. This domain contains a discontinuity surface Γ_c. Compressive displacements $\bar{\boldsymbol{u}}$ are imposed on Γ_u, and tractions $\bar{\boldsymbol{t}}$ are applied on Γ_t, causing the discontinuity surface Γ_c to be in self-contact, and thus the contact forces $\boldsymbol{t}$ between the two sides of the fracture surfaces are non-zero. Ω^+ and Ω^- represent the two bodies separated by the fracture Γ_c. $\boldsymbol{n}_{\Gamma_c}$ is defined as the unit normal of the fracture Γ_c pointing toward Ω^+, and $\boldsymbol{n}_{\Gamma}$ is the unit normal pointing outward from the domain Ω.

2.1. Governing equations

The momentum balance equations and boundary conditions read

$$\boldsymbol{\nabla}\cdot\boldsymbol{\sigma}+\boldsymbol{f}=0 \qquad \text{in } \Omega, \tag{1}$$

$$\boldsymbol{\sigma}\cdot\boldsymbol{n}_{\Gamma_t}=\bar{\boldsymbol{t}} \qquad \text{on } \Gamma_t, \tag{2}$$

$$\boldsymbol{\sigma}\cdot\boldsymbol{n}_{\Gamma_c}=\boldsymbol{t} \qquad \text{on } \Gamma_c, \tag{3}$$

$$\boldsymbol{d}=\bar{\boldsymbol{u}} \qquad \text{on } \Gamma_u, \tag{4}$$

where $\boldsymbol{\sigma}$ is the stress tensor, $\boldsymbol{f}$ is the body force vector, and $\boldsymbol{d}$ is the displacement field over the entire domain. The second-order partial differential equation for the displacement field $\boldsymbol{d}$ is given by

$$\boldsymbol{\nabla}\cdot(\boldsymbol{C}:\boldsymbol{\nabla}^s\boldsymbol{d})+\boldsymbol{f}=0, \tag{5}$$

where $\boldsymbol{\nabla}^s$ denotes the symmetrical part of the gradient operator. $\boldsymbol{C}$ is the linear elastic constitutive tensor as

$$\boldsymbol{C}=\begin{bmatrix}\lambda+2\mu & \lambda & 0\\ \lambda & \lambda+2\mu & 0\\ 0 & 0 & \mu\end{bmatrix}, \tag{6}$$

with λ and μ denoting the Lame's parameters [53]. The strain tensor ε is expressed as

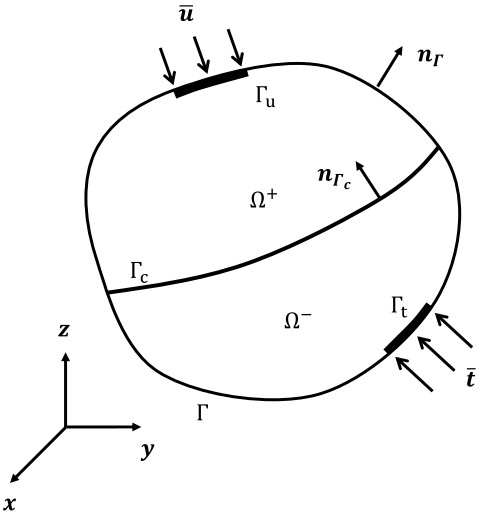

Fig. 1. An illustration of a fractured domain under compression.

$$\boldsymbol{\epsilon} = \boldsymbol{\nabla}^s \boldsymbol{d} = \frac{1}{2}(\boldsymbol{\nabla}\boldsymbol{d} + \boldsymbol{\nabla}^T \boldsymbol{d}), \tag{7}$$

where $\boldsymbol{\nabla}$ denotes the gradient operator, $\boldsymbol{\nabla}^T$ denotes the transpose gradient operator.
The space of admissible displacement fields is given as

$$\mathscr{U} = \{\boldsymbol{d} = \bar{\boldsymbol{u}} \text{ on } \Gamma_u, \boldsymbol{d} \text{ is } C_0 \text{ and discontinuous on } \Gamma_c\}. \tag{8}$$

The test function is then given as

$$\mathscr{U}_0 = \{\boldsymbol{v} = 0 \text{ on } \Gamma_u, \boldsymbol{v} \text{ is } C_0 \text{ and discontinuous on } \Gamma_c\}. \tag{9}$$

The weak form of Eq. (5) is given as

$$\int_\Omega \boldsymbol{\epsilon}(\boldsymbol{v}) : \boldsymbol{\sigma}\, d\Omega + \int_{\Gamma_c} \boldsymbol{t} \cdot [\![\boldsymbol{v}]\!]\, d\Gamma_c = \int_{\Gamma_t} \bar{\boldsymbol{t}} \cdot \boldsymbol{v}\, d\Gamma_t + \int_\Omega \boldsymbol{f} \cdot \boldsymbol{v}\, d\Omega \qquad \forall \boldsymbol{v} \in \mathscr{U}_0, \tag{10}$$

where, the $[\![\boldsymbol{v}]\!]$ represents the difference of test functions across the discontinuity surface Γ_c defined as

$$[\![\boldsymbol{v}]\!] = \boldsymbol{v}_+ - \boldsymbol{v}_-, \tag{11}$$

in which $\boldsymbol{v}_+$ and $\boldsymbol{v}_-$ are the values of the test functions on the fracture surfaces belonging to Ω^+ and Ω^-, respectively.

2.2. Self-contact law

To model the self-contact between two sides of the fracture, first, the displacement difference $[\![\boldsymbol{d}]\!]$ between two sides of fracture Γ_c is defined similarly to Eq. (11) as

$$[\![\boldsymbol{d}]\!] = \boldsymbol{d}_+ - \boldsymbol{d}_-, \tag{12}$$

where $\boldsymbol{d}_+$ and $\boldsymbol{d}_-$ are the displacements on the fracture surfaces that belong to Ω^+ and Ω^-, respectively. The scalar normal gap function, which describes the opening between the two sides of the fracture surfaces, is then defined as

$$g_N = \boldsymbol{n}_{\Gamma_c}^T [\![\boldsymbol{d}]\!], \tag{13}$$

and its vector form, $\boldsymbol{g_N}$, is given as

$$\boldsymbol{g_N} = (\boldsymbol{n}_{\Gamma_c} \otimes \boldsymbol{n}_{\Gamma_c})[\![\boldsymbol{d}]\!], \tag{14}$$

where $(\boldsymbol{n}_{\Gamma_c} \otimes \boldsymbol{n}_{\Gamma_c})$ represents the projection matrix that projects a vector onto the normal direction of the fracture. The scalar tangential gap function, representing the displacement difference along the tangential direction of the fracture surfaces, is defined as

$$g_S = \boldsymbol{m}_{\Gamma_c}^T [\![\boldsymbol{d}]\!], \tag{15}$$

where the $\boldsymbol{m}_{\Gamma_c}$ is the tangential unit vector along the fracture surface. The vector form, $\boldsymbol{g_S}$, is defined as

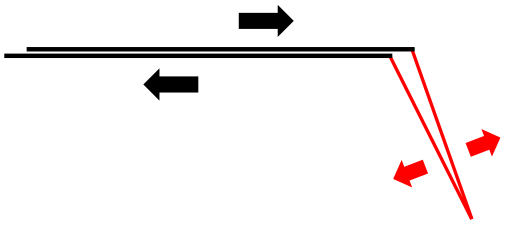

Fig. 2. Illustration showing that the propagation of a fracture tip is induced by shearing along the main body of the fracture. The shear deformation along the initial segment (black) generates forces that lead to the opening of the kinked propagated part (red).

$$\boldsymbol{g_S} = (\boldsymbol{I} - \boldsymbol{n}_{\Gamma_c} \otimes \boldsymbol{n}_{\Gamma_c})[\![\boldsymbol{d}]\!], \tag{16}$$

where $\boldsymbol{I}$ is the identity matrix, and the term $(\boldsymbol{I} - \boldsymbol{n}_{\Gamma_c} \otimes \boldsymbol{n}_{\Gamma_c})$ represents the projection matrix that projects the vector to the tangential direction of fracture.

During the simulation of contact and sliding, strict non-penetration between the two sides of the fractures is enforced. When a gap occurs between fracture surfaces, no contact force is present. However, when two sides of the fracture come into contact, the normal directional contact force scalar t_N becomes negative. The Kuhn-Tucker conditions are used to describe this contact law as follows

$$g_N \geqslant 0, \qquad t_N \leqslant 0, \qquad g_N t_N = 0. \tag{17}$$

In the self-contact problem, the behavior of the sides of the fracture, whether they slide or remain in contact, depends on both external loading and the material-specific frictional coefficient μ_f. This state of sliding or sticking is determined using Coulomb's law of friction, i.e.,

$$t_S + \mu_f t_N \begin{cases} = 0 & \text{slip} \\ < 0 & \text{stick}, \end{cases} \tag{18}$$

where t_S represents the tangential contact force scalar.

2.3. Fracture propagation criterion

Fracture propagation under compressive global loading typically involves mixed-mode failure, as depicted in Fig. 2. The application of compressive outer boundary loading causes the fracture surfaces to come into contact, resulting in non-zero contact forces. Once these fractures are activated, the dominant behavior along the fracture surfaces manifests as slip, indicative of mode-II shearing behavior. This shearing slip can activate the fracture tips to propagate. Notably, the newly propagated segment of the fracture tends to open promptly due to the slip along the original part of the fracture, characterizing this propagation as, essentially, a local mode-I propagation mechanism.

For multiple fractured media, a fracture tip is considered to propagate if the maximum principal stress, σ_1, exceeds the tensile strength of the material σ_t. This is expressed as

$$\sigma_1 > \sigma_t. \tag{19}$$

The propagation speed, or the distance that fracture tips propagate in one time step, is taken as a constant value defined by the user. The propagation angle of the fracture tip is perpendicular to the maximum principal stress around the tip. In this paper, a weighted spatial averaging method is used to compute this angle [54]. In this method, all stress vectors at Gauss points within a circular sector window ahead of the fracture tip are averaged, as illustrated in Fig. 3. The weight of each stress vector at a Gauss point, which contributes to the averaged stress vector, is given by

$$w = \frac{1}{(2\pi)^{\frac{3}{2}} \cdot l^3} \exp(-\frac{r^2}{2l^2}), \tag{20}$$

where l is the radius of the window, typically 3 to 4 times the mesh size, and r is the distance from each Gauss point to the fracture tip. After obtaining the spatially averaged stress vector, the propagation angle is calculated as the direction perpendicular to the maximum principal stress direction of this averaged stress vector.

3. Fine-scale XFEM strategy

Unlike classical FEM, which employs a large number of unstructured grids along fractures and requires remeshing to capture fracture propagation, XFEM can be effectively implemented using static, lower-density structured grids. XFEM introduces enrichment functions to the nodes affected by fractures, as shown in Fig. 4. The fine-scale XFEM simulation strategies for modeling the deformation and propagation of fractured formations will be fully explained below.

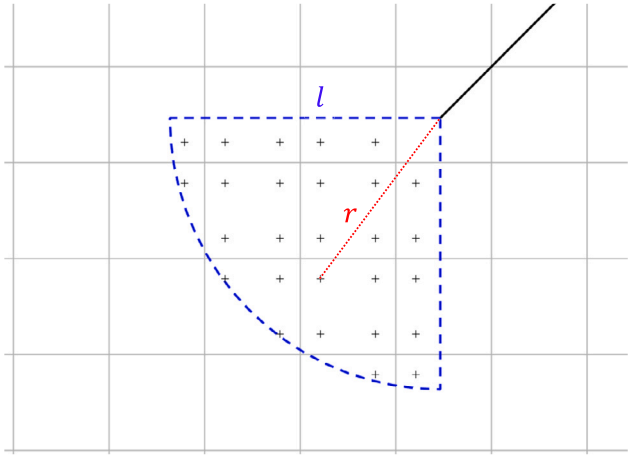

Fig. 3. A sketch of circular sector window. All stress vectors belong to the Gauss points marked with 'plus' signs in the figure are used for weighted spatial average of stress vectors.

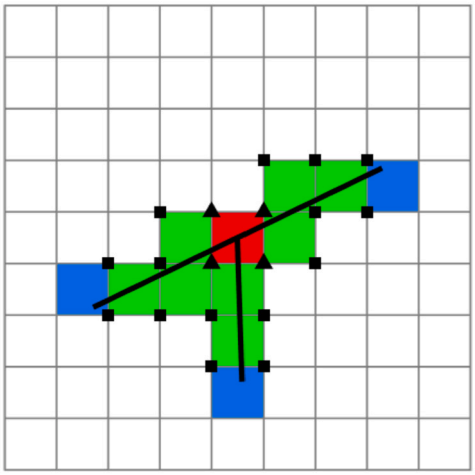

Fig. 4. An illustration of enrichment in XFEM. The black square nodes denote the jump enriched nodes. The black triangle nodes represent the cross enriched nodes. Green colored elements are the elements that are cut through by fractures. Blue colored elements are the elements that contain fracture tips. The red element represents an element intersected by fractures in a crosswise manner. (For interpretation of the colors in the figure(s), the reader is referred to the web version of this article.)

3.1. Extended finite element method

XFEM approximates the displacement field $\boldsymbol{d}$ on a fine-scale mesh Ω^h by $\boldsymbol{d}^h$ which is defined as

$$\boldsymbol{d} \approx \boldsymbol{d}^h = \sum_{i \in \boldsymbol{N_I}} u_i N_i^{st} + \sum_{j \in \boldsymbol{N_E}} a_j N_j^{st} (\mathcal{F}(\boldsymbol{x}) - \mathcal{F}(\boldsymbol{x_c})), \tag{21}$$

where $\boldsymbol{N_I}$ represents all the nodes in the domain while $\boldsymbol{N_E}$ denotes the group of enriched nodes. N_i^{st} and N_j^{st} represent the standard FEM shape functions at nodes i and j, respectively, and $\mathcal{F}$ represents the enrichment functions, which will be defined later. $\boldsymbol{x_c}$ represents the enriched mesh nodes. The multiplication of standard shape functions and enrichment functions results in enriched shape functions, $\boldsymbol{N^{en}}$, which are defined as

$$\boldsymbol{N^{en}} = \boldsymbol{N^{st}} (\mathcal{F}(\boldsymbol{x}) - \mathcal{F}(\boldsymbol{x_c})), \tag{22}$$

where $\boldsymbol{u}$ denotes the standard DOFs associated to the classical finite element method and $\boldsymbol{a}$ denotes the extra DOFs associated to the enriched nodes. The augmented XFEM linear system therefore reads

$$\underbrace{\begin{bmatrix} \boldsymbol{K_{uu}} & \boldsymbol{K_{ua}} \\ \boldsymbol{K_{au}} & \boldsymbol{K_{aa}} \end{bmatrix}}_{\boldsymbol{K}^h} \underbrace{\begin{bmatrix} \boldsymbol{u} \\ \boldsymbol{a} \end{bmatrix}}_{\boldsymbol{d}^h} = \underbrace{\begin{bmatrix} \boldsymbol{f_u} \\ \boldsymbol{f_a} \end{bmatrix}}_{\boldsymbol{f}^h}. \tag{23}$$

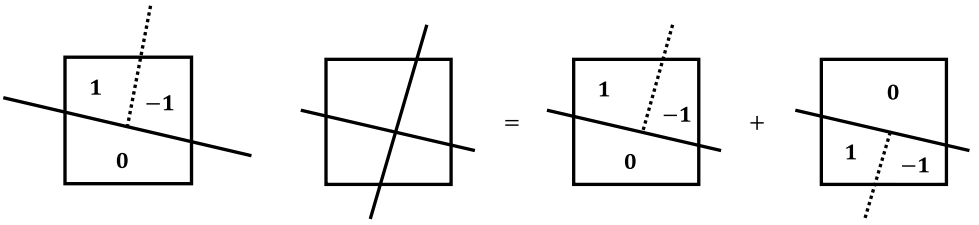

Fig. 5. Two types of the junction enrichment (a) T-shape junction enrichment functions. (b) X-shape junction enrichment subdivided into two T-shape enrichment functions. The solid segment represents the major crack and the dashed segment represents the minor crack.

The strain tensor $\boldsymbol{\varepsilon}$ of Eq. (7) is then expressed as

$$\boldsymbol{\varepsilon} = \boldsymbol{B}^{st}\boldsymbol{u} + \boldsymbol{B}^{en}\boldsymbol{a}, \tag{24}$$

in which the standard strain nodal displacement matrix $\boldsymbol{B}^{st}$ contains derivatives of standard shape functions $\boldsymbol{N}^{st}$ as

$$\boldsymbol{B}^{st} = \begin{bmatrix} \partial N_i^{st}/\partial x & 0 & \dots \\ 0 & \partial N_i^{st}/\partial y & \dots \\ \partial N_i^{st}/\partial y & \partial N_i^{st}/\partial x & \dots \end{bmatrix} \qquad \forall i \in \boldsymbol{N_I}. \tag{25}$$

The enriched matrix $\boldsymbol{B}^{en}$ contains derivatives of enriched shape functions $\boldsymbol{N}^{en}$ as

$$\boldsymbol{B}^{en} = \begin{bmatrix} \partial N_i^{en}/\partial x & 0 & \dots \\ 0 & \partial N_i^{en}/\partial y & \dots \\ \partial N_i^{en}/\partial y & \partial N_i^{en}/\partial x & \dots \end{bmatrix} \qquad \forall i \in \boldsymbol{N_E}. \tag{26}$$

3.2. Enrichment functions

In XFEM, enrichment functions $\mathcal{F}(\boldsymbol{x})$ include jump enrichment functions $H(\boldsymbol{x})$, junction enrichment functions $J(\boldsymbol{x})$, and tip enrichment functions $T(\boldsymbol{x})$. The jump enrichment functions $H(\boldsymbol{x})$ are defined as

$$H(\boldsymbol{x}) = \begin{cases} 1 & \text{on } \Omega^+ \\ -1 & \text{on } \Omega^- \end{cases}. \tag{27}$$

The junction enrichment functions $J(\boldsymbol{x})$ are defined based on different crossing scenarios between fractures. Typically, fractures can intersect in either a T-shape, as shown in Fig. 5(a) or an X-shape, as shown in Fig. 5(b). The details of these two crossing scenarios are thoroughly explained in previous work [49]. The junction enrichment function $J(\boldsymbol{x})$ for a T-shape crossing is then given by

$$J(\boldsymbol{x}) = \begin{cases} H_{II}(\boldsymbol{x}) & H_I(\boldsymbol{x}) > 0 \\ 0 & H_I(\boldsymbol{x}) < 0 \end{cases}, \tag{28}$$

where $H_I(\boldsymbol{x})$ is the jump function value at any Gauss point due to the major crack (the solid segment in Fig. 5(a)), and $H_{II}(\boldsymbol{x})$ is the jump function value due to the minor crack (the dashed segment in Fig. 5(a)). The X-shaped junction enrichment functions are decomposed into two sets of T-shaped enrichment functions, as shown in Fig. 5(b).

In this work, a local-zone tip enrichment, which is more consistent with the jump enrichment, is applied [55]. An example of this local-zone tip enrichment function is illustrated in Fig. 6. A segment EF, parallel to AD and encompassing the fracture tip T, is delineated. Only nodes A and D are affected by this local-zone tip enrichment function, as AD is the boundary cut by the fracture. Notably, only Gauss points situated within the gray-shaded rectangular area $AFED$ will exhibit non-zero values for the local tip enrichment function. The local-zone tip enrichment function is determined as follows: the area $AFED$ is mapped to the reference rectangle $A'F'E'D'$. The Gauss point with coordinates $[\xi, \eta]$ in the original element $ABCD$ is mapped to the corresponding Gauss point in the reference rectangle $A'F'E'D'$ with coordinates $[\xi', \eta']$. The local-zone tip enrichment function at the Gauss point $[\xi, \eta]$ is then computed as

$$T(\xi, \eta) = N^*_{x_n}(\xi', \eta')(H(\xi, \eta) - H(\boldsymbol{x}_c)), \tag{29}$$

where $N^*_{x_n}(\xi', \eta')$ represents the standard shape functions on Gauss point $[\xi', \eta']$ inside the reference rectangle $A'F'E'D'$. $\boldsymbol{x}_c$ are the jump enriched nodes of the element $ABCD$, i.e., AD. $H(\xi, \eta)$ is the jump enrichment function on Gauss point $[\xi, \eta]$ inside the original element $ABCD$ and $H(\boldsymbol{x}_c)$ are the jump enrichment function values on the enriched nodes AD.

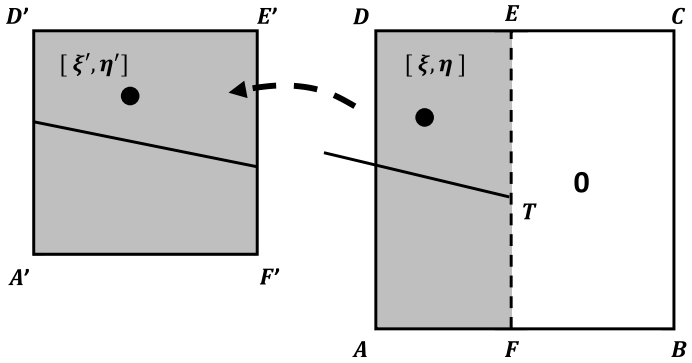

Fig. 6. An illustration of the modified local-zone tip enrichment function. This modified local-zone tip enrichment function only affects in the gray colored zone $AFED$. $A'F'E'D'$ is then transferred reference rectangle of $AFED$.

3.3. Penalty method

The penalty method is often paired with XFEM for simulating self-contact problems. It introduces a penalty term into the problem formulation that penalizes violations of contact constraints. To enforce the contact constraints in Eq. (17), a penalty term is added by incorporating a penalty coefficient into the formulation. This penalty coefficient is a sufficiently large positive number, ensuring satisfaction of the contact constraints. The normal contact force vector acting on the fracture is expressed as

$$\boldsymbol{t}_{\boldsymbol{N}} = C_N \boldsymbol{g}_{\boldsymbol{N}}, \tag{30}$$

where C_N represents the normal directional penalty parameter across the fracture surface, ensuring the prevention of penetration. To compute slip along the fracture surfaces, the tangential force $\boldsymbol{t}_{\boldsymbol{S}}$ along the fracture surface must be determined. The rate of change of the tangential contact force is expressed as

$$\dot{\boldsymbol{t}}_{\boldsymbol{S}} = C_T(\dot{\boldsymbol{g}}_{\boldsymbol{S}} - \dot{S}\frac{\boldsymbol{t}_{\boldsymbol{S}}}{\|\boldsymbol{t}_{\boldsymbol{S}}\|}), \tag{31}$$

where, C_T denotes the penalty parameter along the tangential direction of the fracture. The vector $\dot{\boldsymbol{g}}_{\boldsymbol{S}}$ represents the rate of change of the $\boldsymbol{g}_{\boldsymbol{S}}$ in Eq. (16). $\dot{S}$ represents the slip rate along the fracture surface. Under the "stick" condition, $\dot{S}$ equals 0. Conversely, when "slip" occurs, a return mapping method is employed to calculate the tangential direction contact force in Eq. (31) [50,13].
The return mapping method operates as follows: at iteration i, after obtaining the incremental tangential displacement jump $\Delta \boldsymbol{g}^i_{\boldsymbol{S}}$, which represents $\dot{\boldsymbol{g}_{\boldsymbol{S}}}$ in iteration i, along with the normal displacement jump $\boldsymbol{g}^i_{\boldsymbol{N}}$ and the tangential contact force vector $\boldsymbol{t}^{i-1}_{\boldsymbol{S}}$ from the previous iteration, the predicted updated tangential contact force is calculated as

$$\boldsymbol{t}^{pr,i}_{\boldsymbol{S}} = \boldsymbol{t}^{i-1}_{\boldsymbol{S}} + C_T \cdot \Delta \boldsymbol{g}^i_{\boldsymbol{S}}. \tag{32}$$

If this predicted value adheres to Coulomb's law of friction, as expressed by

$$\|\boldsymbol{t}^{pr,i}_{\boldsymbol{S}}\| - \mu_f \|C_N \cdot \boldsymbol{t}^i_{\boldsymbol{N}}\| \leq 0, \tag{33}$$

it is accepted as the tangential contact force at this iteration $\boldsymbol{t}^i_{\boldsymbol{S}}$. Otherwise, it is corrected to reflect the fact that the fracture is indeed in slip mode. The corrected tangential contact force is equal to the sliding frictional force and is given by

$$\boldsymbol{t}^i_{\boldsymbol{S}} = \mu_f \|C_N \cdot \boldsymbol{t}^i_{\boldsymbol{N}}\| \cdot \frac{\boldsymbol{t}^{pr,i}_{\boldsymbol{S}}}{\|\boldsymbol{t}^{pr,i}_{\boldsymbol{S}}\|}. \tag{34}$$

Note that using return-mapping requires iteratively updating the contact forces.

3.4. Linear system of XFEM with penalty method

As for the linear matrix system, one additional term needs to be added to matrix $\boldsymbol{K}^h$ in Eq. (23) as

$$\boldsymbol{K}^p = \begin{bmatrix} \boldsymbol{K}_{\boldsymbol{uu}} & \boldsymbol{K}_{\boldsymbol{ua}} \\ \boldsymbol{K}_{\boldsymbol{au}} & \boldsymbol{K}_{\boldsymbol{aa}} + \boldsymbol{K}_{\boldsymbol{con}} \end{bmatrix}, \tag{35}$$

where the contact matrix $\boldsymbol{K}_{\boldsymbol{con}}$ is expressed as

$$\boldsymbol{K}_{\boldsymbol{con}} = \int_{\Gamma_c} [\![\boldsymbol{N}^{\boldsymbol{en}}]\!]^T \frac{\partial \boldsymbol{t}}{\partial [\![\boldsymbol{d}]\!]} d\Gamma_c = \int_{\Gamma_c} [\![\boldsymbol{N}^{\boldsymbol{en}}]\!]^T \boldsymbol{D} [\![\boldsymbol{N}^{\boldsymbol{en}}]\!] d\Gamma_c. \tag{36}$$

The term $[\![\boldsymbol{N}^{\boldsymbol{en}}]\!]$ is expressed as

$$[\![\boldsymbol{N}^{en}]\!] = (\boldsymbol{N}_{+}^{en} - \boldsymbol{N}_{-}^{en}), \tag{37}$$

where, $\boldsymbol{N}_{+}^{en}$ and $\boldsymbol{N}_{-}^{en}$ represent the values of the enriched shape functions on the two sides of the fracture surfaces. The $\boldsymbol{D}$ matrix contains the penalty parameters in both normal and tangential directions. Dependent on the stick or slip state, the matrix $\boldsymbol{D}$ can be different. In slip state, the tangential force is equal to the sliding frictional force in Eq. (34) thus in slip state $\boldsymbol{D}$ matrix is

$$\boldsymbol{D} = C_N \cdot (\boldsymbol{n}_{\boldsymbol{\Gamma}_c} \otimes \boldsymbol{n}_{\boldsymbol{\Gamma}_c}) - \mu_f C_N \cdot (\boldsymbol{m}_{\boldsymbol{\Gamma}_c} \otimes \boldsymbol{n}_{\boldsymbol{\Gamma}_c}), \tag{38}$$

and in stick state, $\boldsymbol{D}$ matrix is

$$\boldsymbol{D} = C_N \cdot (\boldsymbol{n}_{\boldsymbol{\Gamma}_c} \otimes \boldsymbol{n}_{\boldsymbol{\Gamma}_c}) + C_T \cdot (\boldsymbol{I} - \boldsymbol{n}_{\boldsymbol{\Gamma}_c} \otimes \boldsymbol{n}_{\boldsymbol{\Gamma}_c}). \tag{39}$$

The return mapping strategy requires an iterative solver. The linear system

$$(\boldsymbol{K}^p)^i \Delta \boldsymbol{d}^{i+1} = \boldsymbol{r}^i \tag{40}$$

is iteratively solved until convergence is reached. Matrix $\boldsymbol{K}^p$ undergoes updates in accordance with the stick-slip conditions observed at the Gauss points on the fractures. The right hand side $\boldsymbol{r}$ in Eq. (40) is expressed as

$$\boldsymbol{r} = \begin{bmatrix} \int_\Gamma (\boldsymbol{N}^{st})^T \cdot \bar{\boldsymbol{t}} d\Gamma + \int_\Omega (\boldsymbol{N}^{st})^T \cdot \boldsymbol{f} d\Omega - \int_\Omega (\boldsymbol{B}^{st})^T \cdot \boldsymbol{\sigma} d\Omega \\ \int_\Gamma (\boldsymbol{N}^{en})^T \cdot \bar{\boldsymbol{t}} d\Gamma + \int_\Omega (\boldsymbol{N}^{en})^T \cdot \boldsymbol{f} d\Omega - \int_\Omega (\boldsymbol{B}^{en})^T \cdot \boldsymbol{\sigma} d\Omega - \int_{\Gamma_c} ([\![\boldsymbol{N}^{en}]\!])^T \cdot \boldsymbol{t} d\Gamma_c \end{bmatrix}. \tag{41}$$

The matrix $\boldsymbol{K}_{con}$ and contact force vector $\boldsymbol{t} = \boldsymbol{t}_T + \boldsymbol{t}_N$ are determined through integration across the Gauss points situated along the fracture segments. Two standard convergence conditions within the outer loops are involved. The first convergence condition is the residual control condition, i.e.,

$$\frac{\|\boldsymbol{r}^i\|}{\|\boldsymbol{r}_0\|} \leqslant \tau_r, \tag{42}$$

and the second one is the displacement incremental control criterion, i.e.,

$$\frac{\|\Delta \boldsymbol{d}^{i+1}\|}{\|\boldsymbol{d}^i\|} \leqslant \tau_d. \tag{43}$$

τ_r and τ_d are the two tolerance values set by the user. The result is considered acceptable if either of these two criteria is met. This algorithm can be found in Algorithm 1 in Appendix A.

3.5. Fractures propagation simulation using level sets functions

In the XFEM community, it is commonly observed that level set functions are incorporated into XFEM to simulate fracture propagation, as they can accurately represent the extension of embedded surface geometries [56,57]. This paper also utilizes level set functions to aid in fracture propagation simulation. At each propagation time step, the displacement is computed following Algorithm 2 in Appendix A and is then used to determine the propagation direction based on the strategy outlined in Section 2.3. The level set functions are subsequently updated using the computed propagation direction and a user-defined length. Further details can be found in the previous work [49].

4. MS-XFEM simulation strategy

From previous section, it is evident that classical XFEM exhibits limitations when applied to the simulation of highly fractured subsurface formations. The excessive number of fractures in the subsurface formation leads to a substantial increase of the number of extra DOFs, thereby expanding the size of the linear system to a point where computational efficiency becomes a significant challenge. To resolve this challenge, a multiscale strategy is incorporated with fine-scale XFEM. This multiscale extended finite element method, or MS-XFEM, will be explained.

4.1. Multiscale simulation strategy

In the multiscale simulation strategy, the fine-scale solution field $\boldsymbol{d}^h$ on the mesh Ω^h can be approximated by $\boldsymbol{d'}^h$, which is interpolated from the coarse-scale solution field $\boldsymbol{d}^H$ on a coarser scale mesh Ω^H. The coarse mesh contains significantly fewer elements compared to the fine-scale mesh, making the computation of the coarse-scale solution $\boldsymbol{d}^H$ less expensive than directly obtaining the fine-scale solution $\boldsymbol{d}^h$ from the fine-scale system in Eq. (23). The coarse-scale mesh is generated on top of the fine-scale mesh, as illustrated in Fig. 7. The coarsening ratio is defined as the ratio between the coarse mesh size and the fine-scale mesh size, which is 4×4 in Fig. 7.
This multiscale formulation is expressed as

$$\boldsymbol{d}^h \approx \boldsymbol{d'}^h = \boldsymbol{P} \cdot \boldsymbol{d}^H, \tag{44}$$

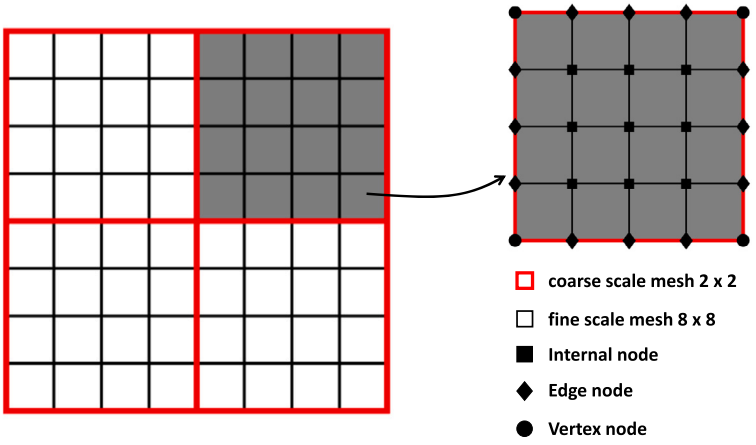

Fig. 7. Illustration of the multiscale mesh imposed on a given fine-scale mesh, with a coarsening ratio of 4×4. The fine-scale mesh nodes in each coarse scale element can be categorized as internal nodes, edge nodes and vertex nodes.

where $\boldsymbol{P}$ is the matrix of basis functions. $\boldsymbol{P}$ has dimensions of $N^h \times N^H$, where N^h is the size of the fine-scale enriched XFEM system, including the extra DOFs, and N^H is the size of the coarse mesh. To construct the coarse-scale system of equations and solve for $\boldsymbol{d}^H$, the fine-scale linear system is restricted to the coarse scale via

$$\underbrace{(\boldsymbol{P}^T \cdot \boldsymbol{K}^p \cdot \boldsymbol{P})}_{\boldsymbol{K}^H} \boldsymbol{d}^H = \boldsymbol{P}^T \cdot \boldsymbol{f}^h, \tag{45}$$

where $\boldsymbol{K}^p$ is defined in Eq. (35). This results in the coarse-scale system matrix $\boldsymbol{K}^H$ of size $N^H \times N^H$. Once the coarse-scale system is solved for $\boldsymbol{d}^H$, the approximate fine-scale solution can be computed using Eq. (44). Overall, the multiscale procedure can be summarized as finding an approximate solution $\boldsymbol{d}'^h$ according to

$$\boldsymbol{d}^h \approx \boldsymbol{d}'^h = \boldsymbol{P}\, \boldsymbol{d}^H = \boldsymbol{P}(\boldsymbol{P}^T\ \boldsymbol{K}^p\ \boldsymbol{P})^{-1} \boldsymbol{P}^T\ \boldsymbol{f}^h. \tag{46}$$

In here, the term $\boldsymbol{P}(\boldsymbol{P}^T\ \boldsymbol{K}^h\ \boldsymbol{P})^{-1} \boldsymbol{P}^T$ is called the multiscale operator $\boldsymbol{M}_{\boldsymbol{MS}}^{-1}$. Once $\boldsymbol{P}$ is constructed, all terms in Eq. (46) are defined.

4.2. Algebraic construction of basis functions

In MS-XFEM, the primary concept behind constructing the basis functions matrix is to incorporate all extra DOFs into the matrix $\boldsymbol{P}$ instead of the coarse-scale solution $\boldsymbol{d}^H$. This approach is crucial for significantly improving computational efficiency, as the coarse-scale system becomes a small, finite-element-like system without extra DOFs. To maintain this structure, the local XFEM problem must be solved within each coarse element. The local equilibrium equation is expressed as

$$\nabla \cdot (\boldsymbol{C} : (\nabla^S \Phi_j^k)) = 0 \qquad \text{in} \quad \Omega_j. \tag{47}$$

Here, Φ_j^k represents the value of the basis function associated with coarse mesh node k in the coarse element Ω_j. A reduced-dimensional equilibrium equation is first solved, and its solution is used as the boundary condition for Eq. (47), i.e.,

$$\nabla_{\parallel} \cdot (\boldsymbol{C}_{\boldsymbol{r}} : (\nabla_{\parallel}^S \Phi_j^k)) = 0 \qquad \text{on} \quad \partial\Omega_j. \tag{48}$$

Here, $\partial\Omega_j$ denotes the boundary of the coarse element Ω_j. Additionally, $\nabla_{\parallel}^S$ represents the reduced-dimensional divergence and symmetric gradient operator, which act parallel to the direction of the local domain boundary. Moreover, $\boldsymbol{C}^R$ is the reduced-dimensional (here, 1D) average elasticity tensor along the boundary of the coarse element, defined as

$$\boldsymbol{C}_x^R = \begin{bmatrix} \bar{\lambda} & 0 & 0 \\ 0 & 0 & 0 \\ 0 & 0 & \bar{\mu} \end{bmatrix} \qquad \boldsymbol{C}_y^R = \begin{bmatrix} 0 & 0 & 0 \\ 0 & \bar{\lambda} & 0 \\ 0 & 0 & \bar{\mu} \end{bmatrix}, \tag{49}$$

where, $\bar{\lambda}$ and $\bar{\mu}$ are averaged elasticity properties of the adjacent 2D elements containing to the same 1D boundary edge.
The construction of basis functions can be done algebraically for convenience. To achieve this, the stiffness matrix needs to be permuted. As shown in Fig. 7, all nodes within any coarse element can be divided into three groups: internal, edge, and vertex nodes. Note that the group of vertex nodes also corresponds to the coarse mesh nodes. The basis functions can then be described as functions that express the values at internal and edge nodes using only the vertex nodes. Therefore, the permutation should be performed based on the locations of fine-scale nodes within the coarse elements. After permutation, the system is expressed as

$$\begin{bmatrix} \boldsymbol{K}^h_{II} & \boldsymbol{K}^h_{IE} & \boldsymbol{K}^h_{IV} \\ \boldsymbol{K}^h_{EI} & \boldsymbol{K}^h_{EE} & \boldsymbol{K}^h_{EV} \\ \boldsymbol{K}^h_{VI} & \boldsymbol{K}^h_{VE} & \boldsymbol{K}^h_{VV} \end{bmatrix} \begin{bmatrix} \boldsymbol{d}^h_I \\ \boldsymbol{d}^h_E \\ \boldsymbol{d}^h_V \end{bmatrix} = \begin{bmatrix} \boldsymbol{f}^h_I \\ \boldsymbol{f}^h_E \\ \boldsymbol{f}^h_V \end{bmatrix}. \tag{50}$$

Here, I represents the internal nodes, E represents the edge nodes, and V represents the vertex nodes. As shown in Fig. 7, the coarse-scale solutions are located at the vertex nodes. The functions that interpolate the solution between the vertex nodes through the edge and internal nodes constitute the necessary basis functions. Note that the fine-scale matrix $\boldsymbol{K}^h$, which is permuted in Eq. (50), does not include the contact matrix $\boldsymbol{K}_{con}$. However, these basis functions will be multiplied by the matrix $\boldsymbol{K}^p$, which includes the sub-matrix $\boldsymbol{K}_{con}$, to obtain the coarse-scale system.

The reduced-dimensional boundary condition in Eq. (48) is now imposed by a 1D XFEM discrete system within the 2D XFEM problem. This causes the entry $\boldsymbol{K}_{EI}$ in Eq. (50) to vanish, as the connectivity between the edge and internal nodes for the edge elements is assumed to be absent. These 1D edge equations can then be expressed as

$$\boldsymbol{K}^R_{EE}\boldsymbol{d}^h_E + \boldsymbol{K}^R_{EV}\boldsymbol{d}^h_V = 0, \tag{51}$$

where, $\boldsymbol{K}^R$ denotes the reduced-order stiffness matrix, employing the $\boldsymbol{C}^R$ matrices as defined in Eq. (49)

$$\boldsymbol{K}^R_m = \int_{\Omega^h} [\boldsymbol{B}^{R,st}_m \ \boldsymbol{B}^{R,en}_m]^T \cdot \boldsymbol{C}^R_m \cdot [\boldsymbol{B}^{R,st}_m \ \boldsymbol{B}^{R,en}_m] d\Omega^h, \ m = x, y. \tag{52}$$

Note that the reduced-dimensional equilibrium equations are solved along the horizontal and vertical boundaries of coarse elements in 2D; thus, $\boldsymbol{K}^R$ is assembled from $\boldsymbol{K}^R_x$ and $\boldsymbol{K}^R_y$. The matrices $\boldsymbol{B}^{R,st}_m$ and $\boldsymbol{B}^{R,en}_m$ contain derivatives of $\boldsymbol{N}_{st}$ and $\boldsymbol{N}_{en}$ in either the x direction or y direction (2D). For example, $\boldsymbol{B}^{R,st}_x$ is

$$\boldsymbol{B}^{R,st}_x = \begin{bmatrix} \partial N^{st}_i/\partial x & 0 & \dots \\ 0 & 0 & \dots \\ 0 & \partial N^{st}_i/\partial x & \dots \end{bmatrix}. \tag{53}$$

After assembling the $\boldsymbol{K}^R$ matrix, it will be permuted similar to Eq. (50). Then the edge terms $\boldsymbol{K}_{EI}$, $\boldsymbol{K}_{EE}$ and $\boldsymbol{K}_{EV}$ in the permuted stiffness matrix will subsequently be substituted with the corresponding edge terms in the permuted $\boldsymbol{K}^R$. Since the solutions at vertex nodes will be obtained from the coarse-scale system, the reordered fine-scale matrix can now be reduced to

$$\begin{bmatrix} \boldsymbol{K}_{II} & \boldsymbol{K}_{IE} & \boldsymbol{K}_{IV} \\ 0 & \boldsymbol{K}^R_{EE} & \boldsymbol{K}^R_{EV} \\ 0 & 0 & \boldsymbol{K}^H \end{bmatrix} \begin{bmatrix} \boldsymbol{d}'_I \\ \boldsymbol{d}'_E \\ \boldsymbol{d}'_V \end{bmatrix} = \begin{bmatrix} \boldsymbol{0} \\ \boldsymbol{0} \\ \boldsymbol{f}^H \end{bmatrix}, \tag{54}$$

where, $\boldsymbol{d}'_I$, $\boldsymbol{d}'_E$ and $\boldsymbol{d}'_V$ are the approximated displacements solutions for the internal nodes, edge nodes and vertex nodes. Given the coarse nodes solutions $\boldsymbol{d}'_V$, one can obtain the solution at the edge via

$$\boldsymbol{d}'_E = -(\boldsymbol{K}^R_{EE})^{-1}\boldsymbol{K}^R{}_{EV}\ \boldsymbol{d}'_V = \boldsymbol{P}_{EV}\ \boldsymbol{d}'_V. \tag{55}$$

Similarly, the solution at the internal cells reads

$$\begin{aligned} \boldsymbol{d}'_I &= -\boldsymbol{K}^{-1}_{II}(\boldsymbol{K}_{IE}\boldsymbol{d}'_E + \boldsymbol{K}_{IV}\boldsymbol{d}'_V) \\ &= -\boldsymbol{K}^{-1}_{II}(-\boldsymbol{K}_{IE}(\boldsymbol{K}^R_{EE})^{-1}\boldsymbol{K}^R{}_{EV} + \boldsymbol{K}_{IV})\ \boldsymbol{d}'_V = \boldsymbol{P}_{IV}\ \boldsymbol{d}'_V. \end{aligned} \tag{56}$$

The basis function matrix $\boldsymbol{P}$ is then defined as

$$\boldsymbol{d}' = \begin{bmatrix} \boldsymbol{d}'_I \\ \boldsymbol{d}'_E \\ \boldsymbol{d}'_V \end{bmatrix} = \underbrace{\begin{bmatrix} \boldsymbol{P}_{IV} \\ \boldsymbol{P}_{EV} \\ \boldsymbol{I}_{VV} \end{bmatrix}}_{\boldsymbol{P}} \boldsymbol{d}'_V. \tag{57}$$

Here, $\boldsymbol{I}_{VV}$ is the diagonal identity matrix equal to the size of the number of vertex nodes. An illustration of a basis function obtained using this algebraic construction approach is presented in Fig. 8. Note that the illustrated basis function captures the discontinuities due to fracture.

4.3. Algebraic update of basis functions locally

The propagation of fracture tips induces alterations in the geometries of fine-scale fractures, necessitating the incorporation of these changes into the basis functions within MS-XFEM. The basis functions can be updated algebraically and locally. Fig. 9 illustrates how to update basis functions locally. As the horizontal fracture (white-colored segment) propagates, the local domain containing five coarse elements at the center of the entire domain is affected. Only the basis functions within this local domain require updating. To accomplish this, the local basis functions matrix associated with this domain is first extracted. Based on the new geometry of

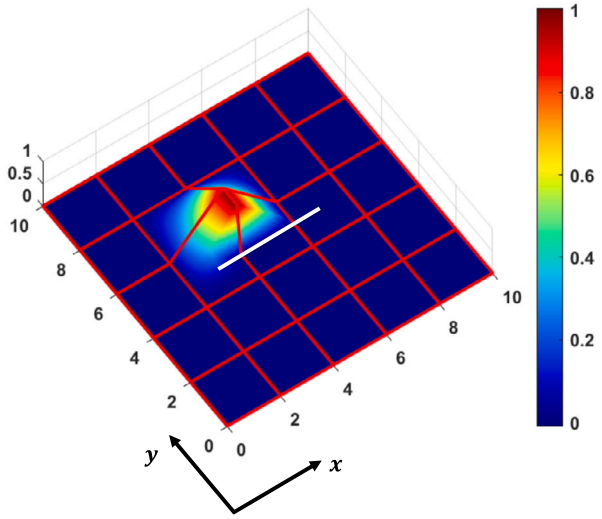

Fig. 8. Illustration of a basis function that captures the discontinuity of a fracture. Model size is $10[m] \times 10[m]$. Red lines represent the coarse scale mesh of 5×5. White segment represents the fracture extending from $(3,5)$ to $(7,5)$. The shown basis function belongs to the coarse node located at coordinate $(4,6)$.

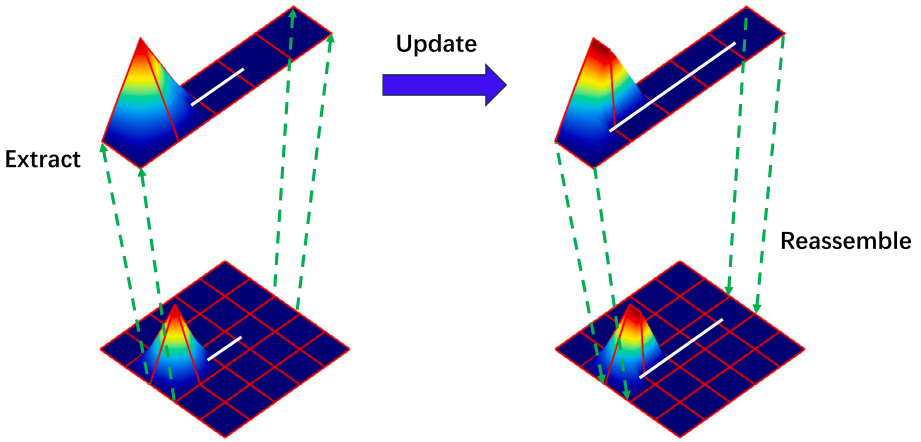

Fig. 9. Illustration of updating basis functions algebraically and locally.

the propagated fracture, this local basis functions matrix is then updated by algebraically computing the new basis function values, following the same strategy as explained above. Finally, this updated local basis functions matrix is reassembled into the global basis functions matrix. This algebraic and local update strategy reduces the computational burden during fracture propagation simulations.

4.4. Iterative strategy of MS-XFEM

Right preconditioned GMRES is used to control the error and reduce it to a desired tolerance [58]. A fine-scale smoother $\boldsymbol{M}_{sm}^{-1}$ (usually chosen as $ILU(0)$) is paired with the multiscale operator $\boldsymbol{M}_{MS}^{-1}$. The preconditioner used here involves the multiscale operator and the fine-scale smoothing operator following

$$\boldsymbol{M}^{-1} = \boldsymbol{M}_{MS}^{-1} + \boldsymbol{M}_{sm}^{-1}(\boldsymbol{I} - \boldsymbol{K}^{p}\ \boldsymbol{M}_{MS}^{-1}). \tag{58}$$

Thus, in any iteration i mentioned in Eq. (40), the displacement field is updated by iteratively solving the following system until convergence:

$$(\boldsymbol{K}^{p})^{i}\,\boldsymbol{M}^{-1}\boldsymbol{z}' = \boldsymbol{r}^{i}, \quad \text{with} \quad \boldsymbol{\Delta d}^{i+1} = \boldsymbol{M}^{-1}\boldsymbol{z}' \tag{59}$$

The preconditioned GMRES tolerance is set by the user. The algorithms for using MS-XFEM to simulate deformations and fracture propagation are presented in Algorithm 3 and Algorithm 4 in Appendix B.

Table 1
Test case 1: domain properties.

		unit	value
L	length	[m]	4
W	width	[m]	2
E	Young's modulus	[Pa]	10^5
μ_f	frictional coefficient	[-]	0.1
ν	Poisson's ratio	[-]	0.3
C_N, C_T	penalty parameters	[N/m^3]	10^7

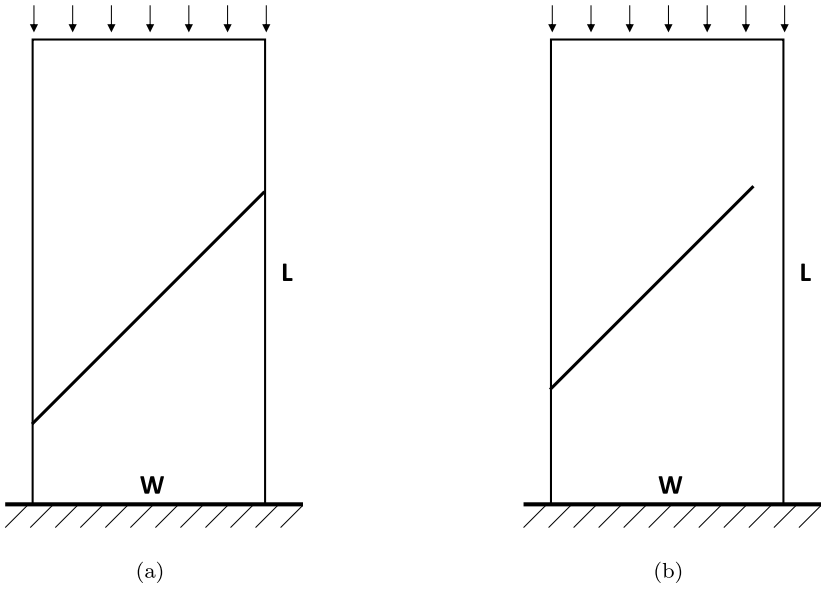

Fig. 10. Test case 1: illustration of two scenarios of cracked domain (a) fully cracked and (b) partially cracked.

5. Test cases

The efficiency of the MS-XFEM method has been analyzed in previous work [48]. It is important to note that MS-XFEM becomes efficient only when the research domain is large and contains extremely complex fracture networks, i.e., when the final solutions involve a massive number of DOFs. In this paper, simpler test cases are designed to demonstrate the capability of MS-XFEM in simulating complex fracture networks under compression, as this is the primary focus of this study. In this section, four test cases are presented to illustrate the application of MS-XFEM for simulating deformation and fracture propagation in mixed mode under compressive loading are presented. Two convergence tolerance values, τ_r and τ_d, are set to 10^{-6} and 10^{-3}, respectively.

5.1. Test 1: slip along edge-inclined crack

In this test case, the accuracy of the slip profiles simulated by MS-XFEM is verified by comparison with the slip profile results presented in [51]. A cracked homogeneous domain is considered here. The properties of this domain are listed in Table 1. The top boundary is subjected to a downward Dirichlet boundary condition of 0.1 [m], while the bottom boundary is fixed in both the x and y directions. The left and right boundaries are stress-free. Here, the fine-scale mesh is set to 40×80, while the coarse-scale mesh is set as 4×8, employing a coarsening ratio of 10×10.

First, the crack is assumed to cut through the entire domain, as shown in Fig. 10(a). The coordinates of the fracture are given as $[0, 0.7]$ and $[2, 2.7]$. For this setup, the slip along the crack follows a uniform profile with constant value of $0.1\sqrt{2}$, or 0.1414. The simulated slip profile using MS-XFEM closely matches this value, as shown in Fig. 11. Note that no iterative improvement strategy is used here, which demonstrates the correctness of constructing basis functions without a penalty matrix.

Next, the crack is assumed to partially cut through the domain, as shown in Fig. 10(b). The coordinates of the fracture are given as $[0, 1]$ and $[1.75, 2.75]$. Here, a non-uniform slip profile is obtained, as presented in [51], and this result is shown in Fig. 12(a). To obtain this non-uniform slip profile, an iterative improvement strategy is required. The tolerance for the preconditioned GMRES is set to 10^{-2} to reduce the number of iterations required by the iterative strategy. The slip profiles simulated using fine-scale XFEM and MS-XFEM are plotted in Fig. 12(b). The MS-XFEM slip profile closely matches the result shown in Fig. 12(a), demonstrating its capability to accurately simulate the deformation of fractured formations.

The convergence history of the preconditioned GMRES in each outer loop (line 3 of Algorithm 3 in Appendix B) is plotted in Fig. 13(a). The total number of preconditioned GMRES used here is 90. Additionally, the convergence history for a tolerance of 10^{-6} is presented

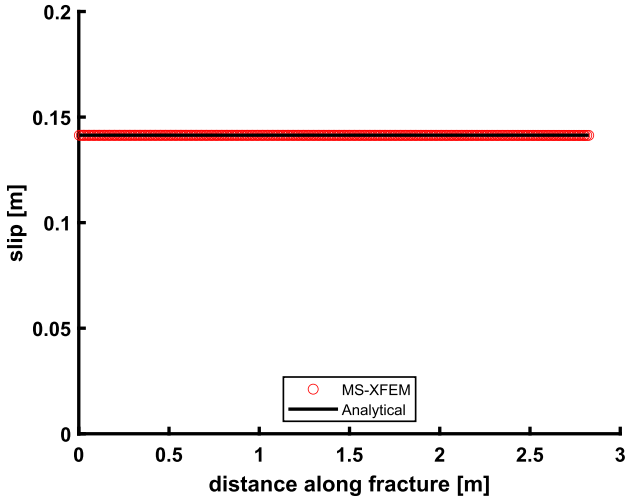

Fig. 11. Test case 1: slip profile computed by analytical method (black curve) and MS-XFEM method without iterative smoother (red curve with circle markers).

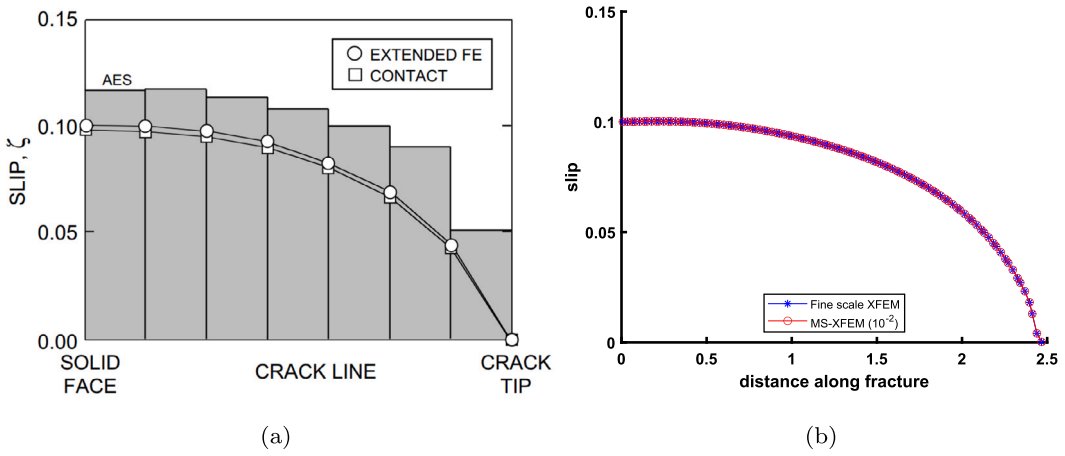

Fig. 12. Test case 1: (a) non-uniform slip profile simulated in [51] (b) slip profile computed by fine-scale XFEM (blue) and MS-XFEM method with a tolerance of 10^{-2} (red).

in Fig. 13(b). The comparison between Fig. 13(a) and Fig. 13(b) indicates that MS-XFEM can achieve high-quality results without incurring excessive computational costs in the iterative improvement strategy.

5.2. Test 2: wing crack propagation in uni-axial compression

In this test case, a rectangular granite sample under uni-axial compression is simulated using MS-XFEM. This test is based on the experimental study reported in [59]. The setup is shown in Fig. 14. The fracture is 6 [mm] long and is rotated by α degrees with respect to the x-axis and located at the center of the sample. The properties of this domain are listed in Table 2. The lower-left corner is fixed in x and y directions, while the remaining nodes along the bottom boundary are restricted solely in y-direction. At the upper boundary, a controlled downward displacement condition is enforced at a rate of 0.1 [mm/s]. Lastly, the left and right boundaries are stress-free. The entire simulation duration spans 10 [s] and is discretized into 10 equal time steps, each lasting 1 [s]. For each step, the fracture propagation length is set to be 1.5 times the element size. The fine-scale mesh is defined as 30×60, while the coarse-scale mesh is set to 3×6. Within this context, preconditioned GMRES iterations are employed with a tolerance threshold of 10^{-2}.
To evaluate the accuracy of the final result, a direct comparison is conducted between the major wing crack propagation paths simulated using fine-scale XFEM and those obtained in the experimental study from literature [59]. This analysis involves three different rotation angles: $\alpha = \pi/6, \pi/4, \pi/3$. The results are depicted in Fig. 15. The red-colored crack paths represent simulations conducted with fine-scale XFEM and are superimposed onto images extracted from the experimental study in [59]. The black-colored paths labeled with 'T' denote the tensile wing cracks observed during the experiment. It is important to note that these labels are assigned numerical identifiers, indicating that these tensile wing cracks did not initiate simultaneously. In this particular test case, the branching of wing cracks is not considered; instead, the primary focus lies on the propagation of the major wing crack. Therefore, the experimental wing crack path labeled as 'T1', representing the initial major wing crack path, is selected as the reference for

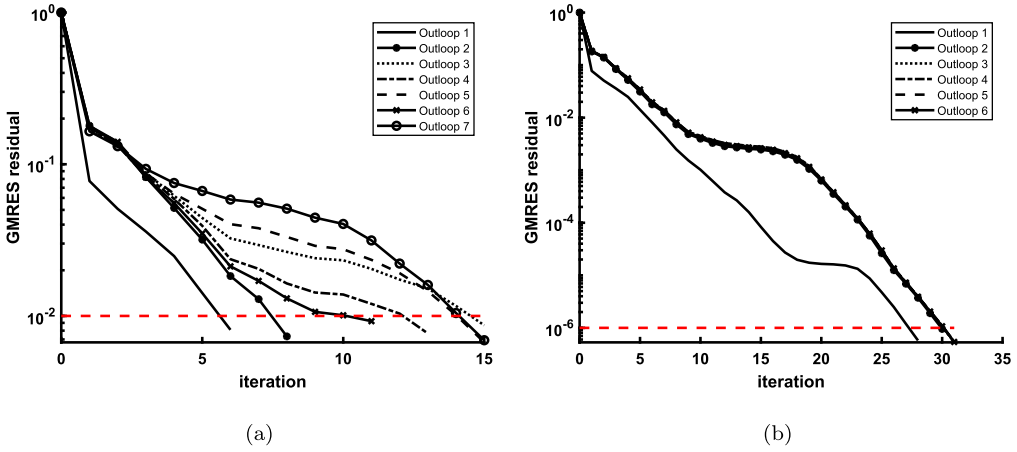

Fig. 13. Test case 1: preconditioned GMRES convergence history with tolerance of (a) 10^{-2} and (b) 10^{-6}.

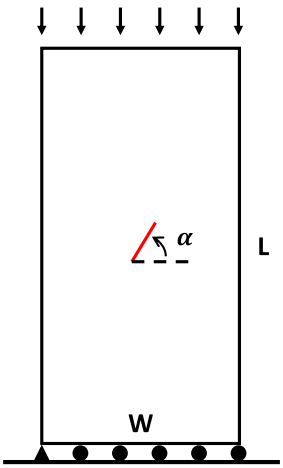

Fig. 14. Test case 2: illustration of the model set-up.

Table 2
Test case 2: domain properties.

		unit	value
L	length	[mm]	120
W	width	[mm]	60
E	Young's modulus	[Pa]	62×10^9
μ_f	frictional coefficient	[-]	0.577
ν	Poisson's ratio	[-]	0.22
C_N, C_T	penalty parameters	[N/m^3]	62×10^{11}
σ_t	tensile strength	[Pa]	16×10^6

comparison with the simulated crack propagation paths. It is evident that for all three tests with varying inclination angles, the simulated major wing crack paths closely resemble the dominant cracks in the experiment.

If the crack paths simulated using MS-XFEM closely resemble those generated by fine-scale XFEM, it indicates that MS-XFEM can produce sufficiently accurate results. The crack paths simulated with MS-XFEM (utilizing preconditioned GMRES) for all three inclined angles are compared to the crack paths shown in Fig. 15 and are presented in Fig. 16. The figure clearly demonstrates a high degree of alignment between the crack paths simulated with MS-XFEM (with GMRES) and those obtained through fine-scale XFEM.

In Fig. 17, the x directional displacement from fine scale XFEM and MS-XFEM with inclination angle of $\pi/6$ are plotted. The error plot between these two displacements fields is also plotted in Fig. 17(c). A total of 333 iterations of preconditioned GMRES over 10 time steps, averaging 33 iterations per time step, were performed to reduce the error in the MS-XFEM results. The basis functions for the coarse mesh node at coordinates $[0.02, 0.04]$, at both step 1 and step 6, are depicted in Fig. 18. It is evident that the update of basis functions has been successful in capturing the propagating fracture tip.

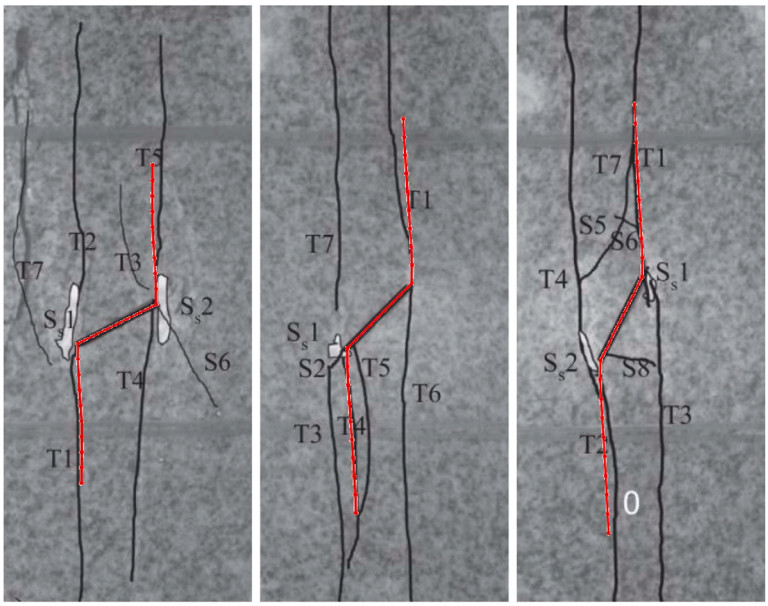

(a) $\pi/6$ (b) $\pi/4$ (c) $\pi/3$

Fig. 15. Test case 2: crack paths simulated using fine-scale XFEM are compared to experimental crack paths for various inclination angles: (a) $\pi/6$, (b) $\pi/4$, and (c) $\pi/3$. The red lines represent crack paths simulated with fine-scale XFEM, while the black-colored crack paths labeled with 'T' on the experimental images denote the major wing cracks. The gray background images are sourced from [59].

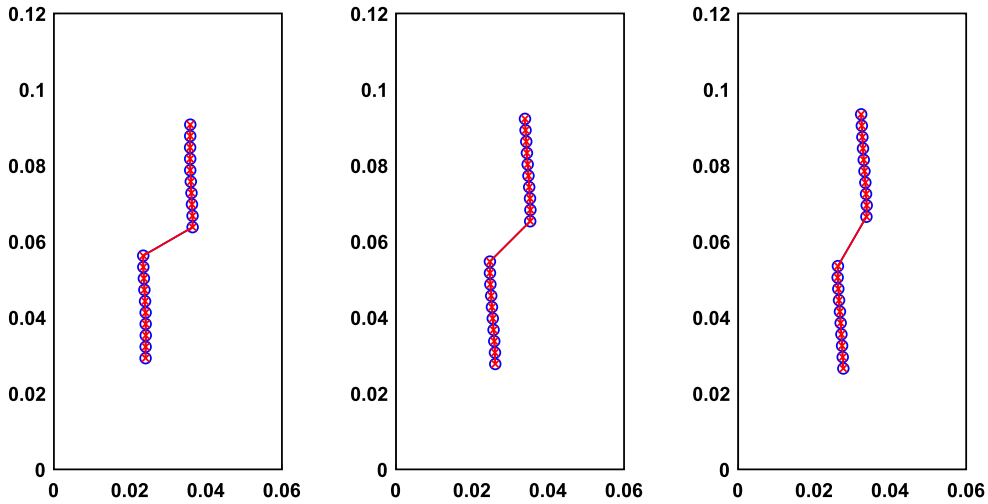

(a) $\pi/6$ (b) $\pi/4$ (c) $\pi/3$

Fig. 16. Test case 2: Crack paths simulated with MS-XFEM compared to the crack patterns generated by fine-scale XFEM. The inclination angles are (a) $\pi/6$, (b) $\pi/4$, and (c) $\pi/3$. The blue circles represent the crack paths simulated with fine-scale XFEM, while the red lines represent the crack patterns from MS-XFEM.

5.3. Test 3: fracture network slip in heterogeneous formation

In this test case, a synthetic fracture network under compression is considered. Fig. 19(a) provides a visual representation of the synthetic fracture network within this domain. The fracture coordinates are listed in Table C.5 in Appendix C. The research domain properties are listed in Table 3. Heterogeneous Young's modulus values, following a Gaussian distribution, are spatially mapped across the entire domain, as shown in Fig. 19(b). The penalty parameters, C_T and C_N, are adjusted for each element due to the varying Young's modulus values in the domain. Specifically, these penalty parameters are set to be 100 times the local Young's modulus of each element.

The fine-scale mesh is set to 80×80 and the coarse mesh is set to 8×8. The bottom boundary is fixed in y-direction, while the left and right boundaries are fixed in x-direction. The top boundary is subjected to displacement-controlled compression of 1[m] downward. For this complex test case, preconditioned GMRES is paired with MS-XFEM. The tolerance for MS-XFEM is set to 10^{-2}.

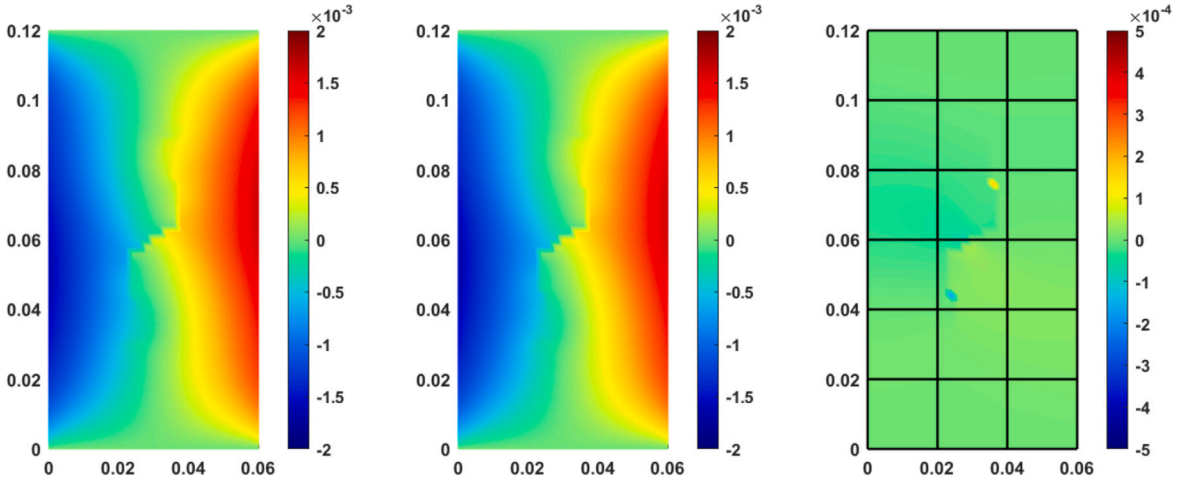

(a) d_x fine-scale XFEM (b) d_x MS-XFEM (c) error in d_x

Fig. 17. Test case 2: x direction displacement of (a) fine scale XFEM and (b) MS-XFEM. The error plot between these two results is shown in (c).

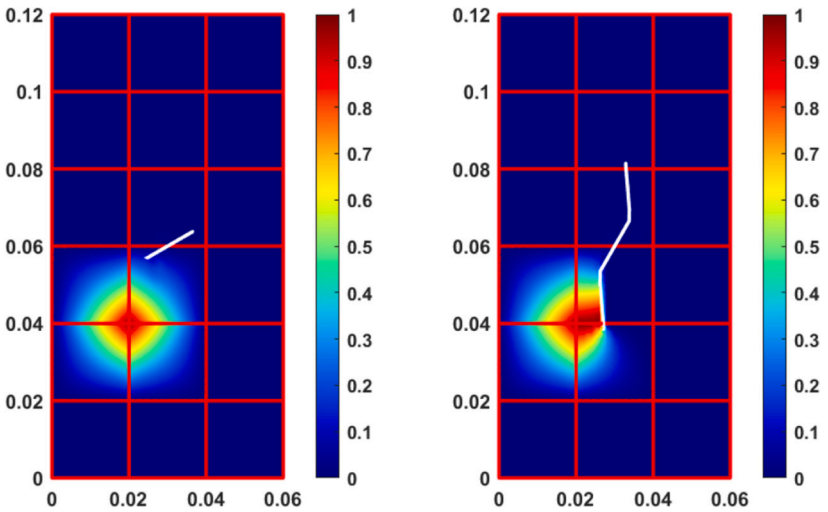

(a) P_{yy} at step 1 (b) P_{yy} at step 6

Fig. 18. Test case 2: basis functions of coarse mesh point $[0.02, 0.04]$ at step (a) 1 and (b) step 6. Red lines represent the coarse mesh and white segment represents the fracture.

Table 3
Test case 3: domain properties.

		unit	value
L	length	[m]	80
W	width	[m]	80
μ_f	frictional coefficient	[-]	0.1
ν	Poisson's ratio	[-]	0.3

The displacements simulated by MS-XFEM closely match those obtained from fine-scale XFEM as shown in Fig. 20. With a total 250 of preconditioned GMRES iterations used, MS-XFEM obtains a reasonably high quality result for this complex fracture network. The error plots in Fig. 21 confirm this accuracy.

Slip profiles of fractures 1, 2, and 8, marked in Fig. 19(a), are plotted in Fig. 22. The most slip occurs along major fracture 2 within the formation. This underscores the importance of closely monitoring slip events along this major fault due to their potential to cause significant surface subsidence. The dashed boxes in each slip profile plot indicate the fracture crossing points. Note that there

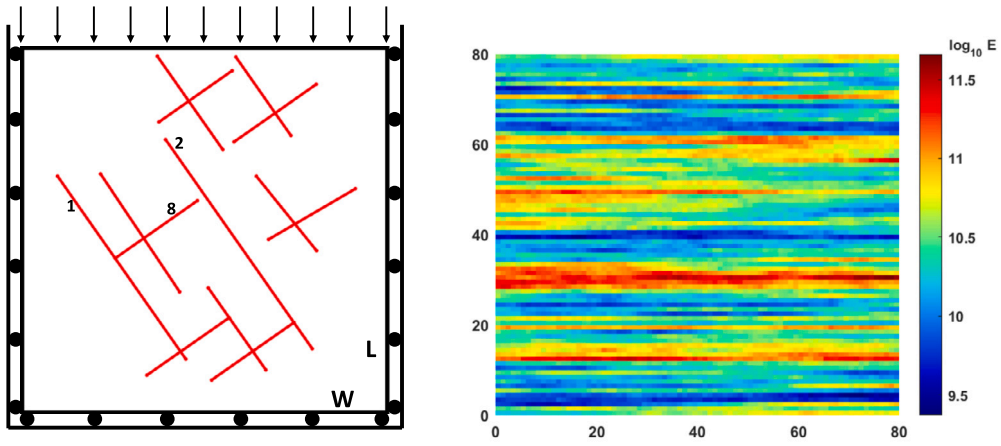

(a) (b)

Fig. 19. Test case 3: (a) illustration of test case 3 set-up (b) Gaussian distributed heterogeneous Young's modulus map.

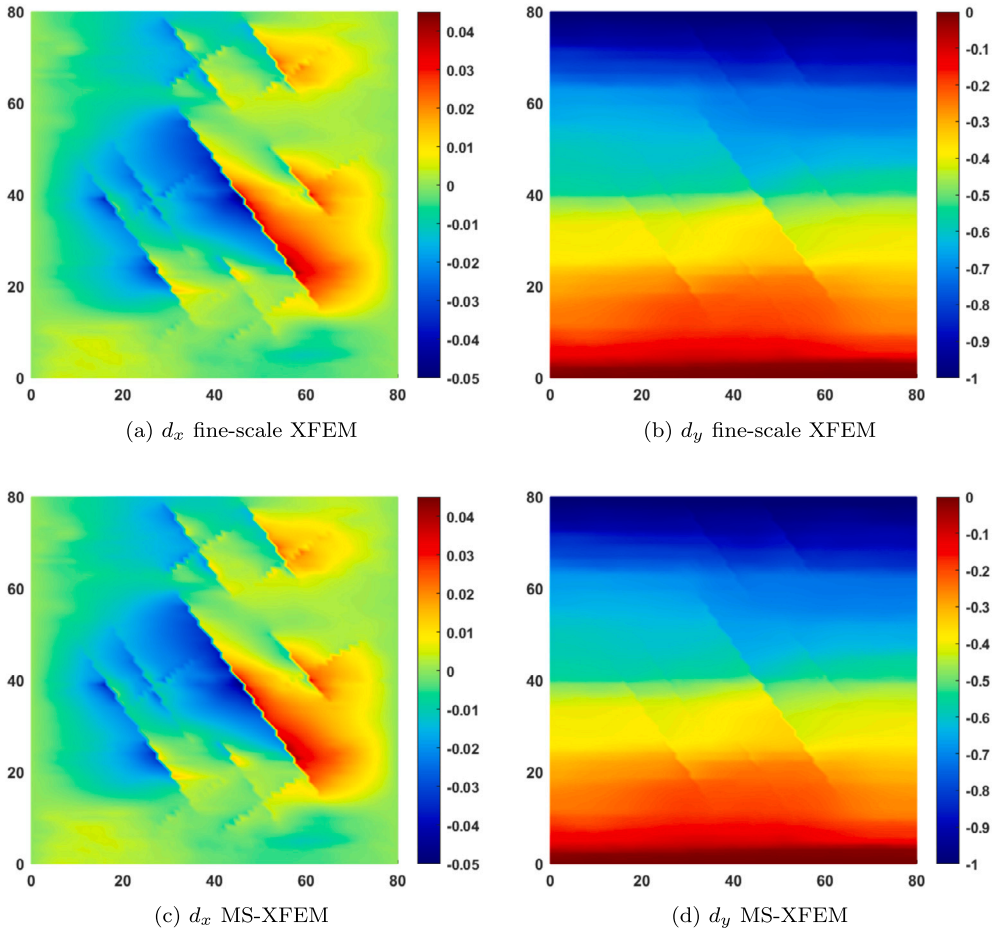

(a) d_x fine-scale XFEM (b) d_y fine-scale XFEM

(c) d_x MS-XFEM (d) d_y MS-XFEM

Fig. 20. Test Case 3: Comparison between displacement solutions from fine-scale XFEM and MS-XFEM. (a) and (b) show displacement fields in the x-direction and y-direction, respectively, using fine-scale XFEM. (c) and (d) show displacement fields in the x-direction and y-direction, respectively, using MS-XFEM.

are oscillations in the slip profiles along the fractures, which is common in XFEM when using standard bi-linear shape functions. A smoothing strategy can be found in [60], but this is beyond the scope of this work. It can be observed that there are kinks in the slip profiles at the crossing points on the fractures, which is consistent with the results in [28]. This demonstrates the potential of

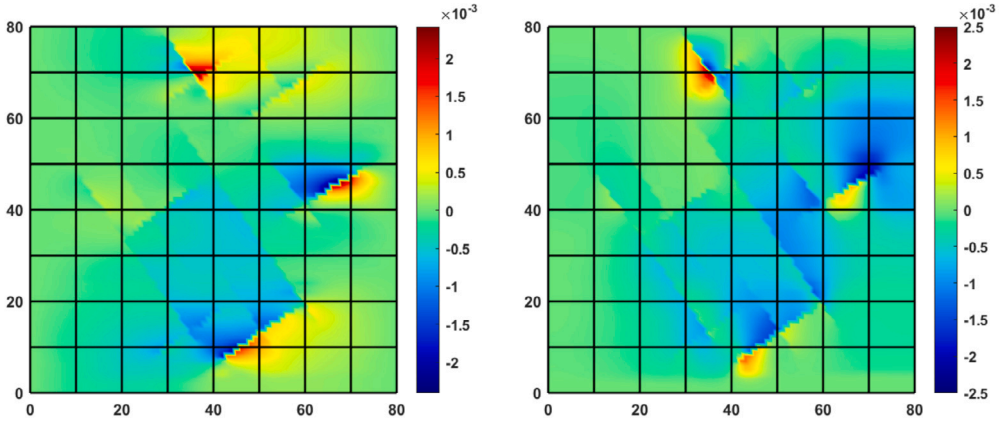

(a) e_x (b) e_y

Fig. 21. Test Case 3: Errors between solutions from fine-scale XFEM and MS-XFEM in (a) the x-direction and (b) the y-direction.

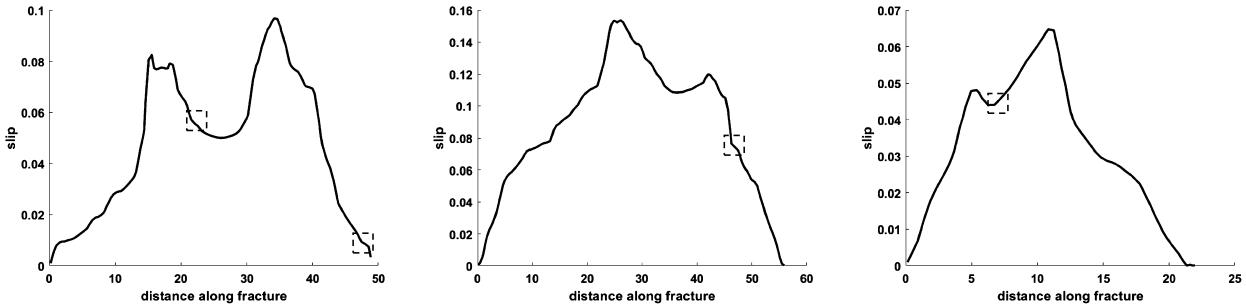

(a) fracture 1 (b) fracture 2 (c) fracture 8

Fig. 22. Test Case 3: Slip profiles along fractures (a) 1, (b) 2, and (c) 8. Dashed boxes represent the crossing points on each fracture.

Table 4
Test case 4: Domain properties.

		unit	value
L	length	[m]	10
W	width	[m]	10
E	Young's modulus	[Pa]	25×10^9
μ_f	frictional coefficient	[-]	0.577
ν	Poisson's ratio	[-]	0.23
C_N, C_T	penalty parameters	[N/m^3]	25×10^{11}
σ_t	tensile strength	[Pa]	6×10^6

MS-XFEM in accurately simulating slip in fracture networks.
In this test case, the basis functions must capture both heterogeneities and multiple fractures simultaneously. The basis functions P_{yy} corresponding to the coarse grid points $[10, 10]$ and $[30, 30]$ are plotted in Fig. 23. It is clear from Fig. 23(a) that the basis functions capture the heterogeneities within the Young's modulus map, as they do not follow the standard bi-linear form. Fig. 23(b) illustrates that the basis functions also successfully capture multiple discontinuities.

5.4. Test 4: multiple fractures propagation under compression

In this test, a sandstone domain with 9 fractures under compression loading is simulated, as shown in Fig. 24. All 9 fractures have the same length of 1[m] and their coordinates are listed in Table C.6 in Appendix C. The domain and material properties are provided in Table 4. For the boundary conditions, the lower-left corner of the domain is fixed, while the nodes along the bottom boundary are constrained only in the vertical direction. A downward distributed load q is applied to the top boundary. The initial value of q is 100 [MPa], increasing by 2 [MPa] at each time step. The simulation spans a total time of 25 seconds, with each time step lasting 1 second. For each step, the fracture propagation length is set to be 2 times the element size.
The fine-scale mesh employed consists of a grid with dimensions of 50×50, while the coarse mesh employs a 5×5 grid. Preconditioned GMRES is utilized for the simulation, with a specified tolerance of 10^{-2}.

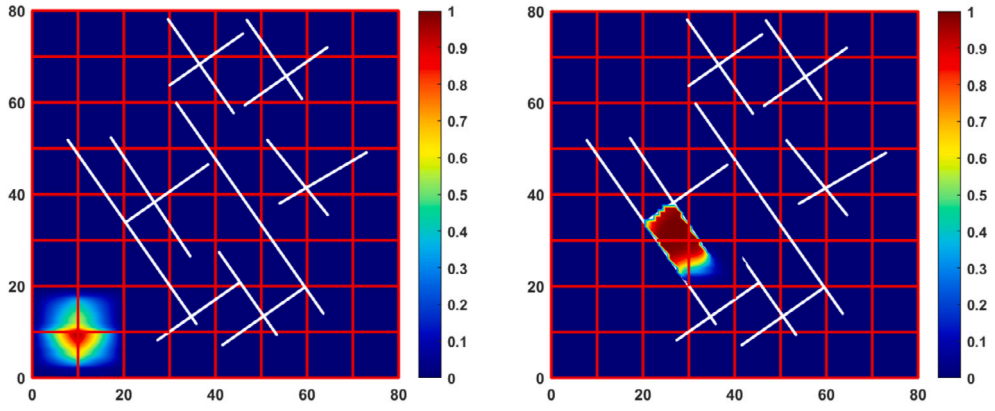

(a) P_{yy} belongs to $[10, 10]$ (b) P_{yy} belongs to $[30, 30]$

Fig. 23. Test Case 3: Basis functions P_{yy} corresponding to the coarse-scale mesh nodes at (a) $[10, 10]$ and (b) $[30, 30]$.

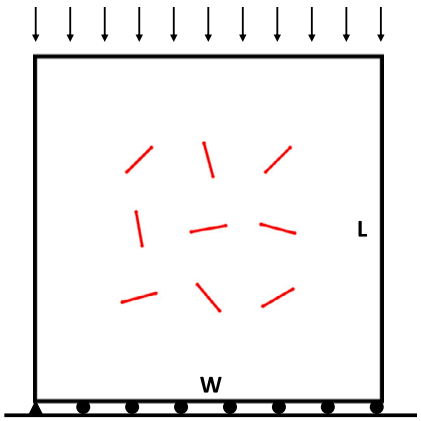

Fig. 24. Test case 4: Illustration of the model set-up.

The crack propagation paths at steps 6 and 25 are illustrated in Fig. 25. The crack paths simulated using MS-XFEM are superimposed on those obtained with fine-scale XFEM. It is evident from Fig. 25 that these paths closely match, validating the accuracy of the MS-XFEM simulations in multiple fractures propagation under compression.

The displacement fields in the x and y directions at the final step are visualized in Fig. 26. Notably, the results obtained from MS-XFEM closely align with those from fine-scale XFEM. To further illustrate this agreement, the displacement errors between the two methods are depicted in Fig. 27. By employing a total of 1851 iterations of preconditioned GMRES over 25 steps, averaging 74 iterations per time step, the errors in the final displacement solution are effectively reduced to the desired level. The basis functions centered at the coarse mesh point $[4, 8]$ at initial time step and time step 11 are displayed in Fig. 28. Clearly, the basis functions update has effectively captured the fracture propagation.

6. Conclusion

This work successfully extends MS-XFEM for simulating frictional slip as well as fracture propagation within subsurface fractured formations. The penalty method is employed to prevent penetration between fracture surfaces by assigning an artificially high stiffness to the cracked elements. A return-mapping method, following Coulomb's law of friction, is applied to determine the slip-stick conditions along the fracture surfaces. The weighted spatial averaging method is used to ensure smooth crack propagation paths in mixed mode under compression. In the application of MS-XFEM, basis functions are constructed algebraically and incorporate all extra DOFs from fine-scale XFEM solutions. The coarse-scale system is then generated as a standard, small-sized FEM-type system, which is highly efficient to compute. To reduce computational time, basis functions are not updated during the return-mapping iterative solution process. However, when fractures propagate, basis functions are updated locally to capture the extension of discontinuities. An iterative improvement strategy, employing preconditioned GMRES, is coupled with MS-XFEM to enhance the accuracy of the final solutions to the desired level.

The successful construction of basis functions is evident, particularly in the first test case, where simple constant slip profile is accurately captured using only MS-XFEM without the iterative improvement strategy. The basis function update strategy is validated in

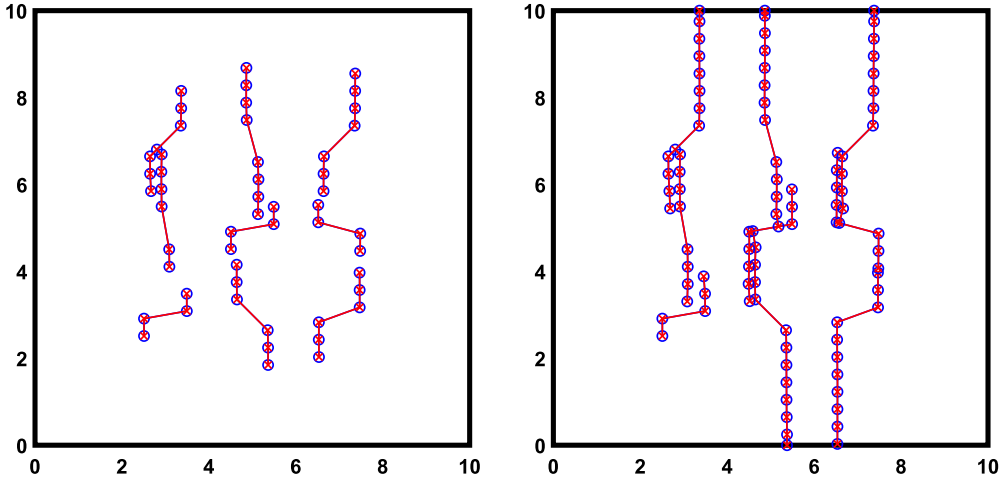

Fig. 25. Test case 4: Crack patterns simulated by fine scale XFEM (blue circles) and MS-XFEM (red crosses) at time step (a) 6 and (b) 25.

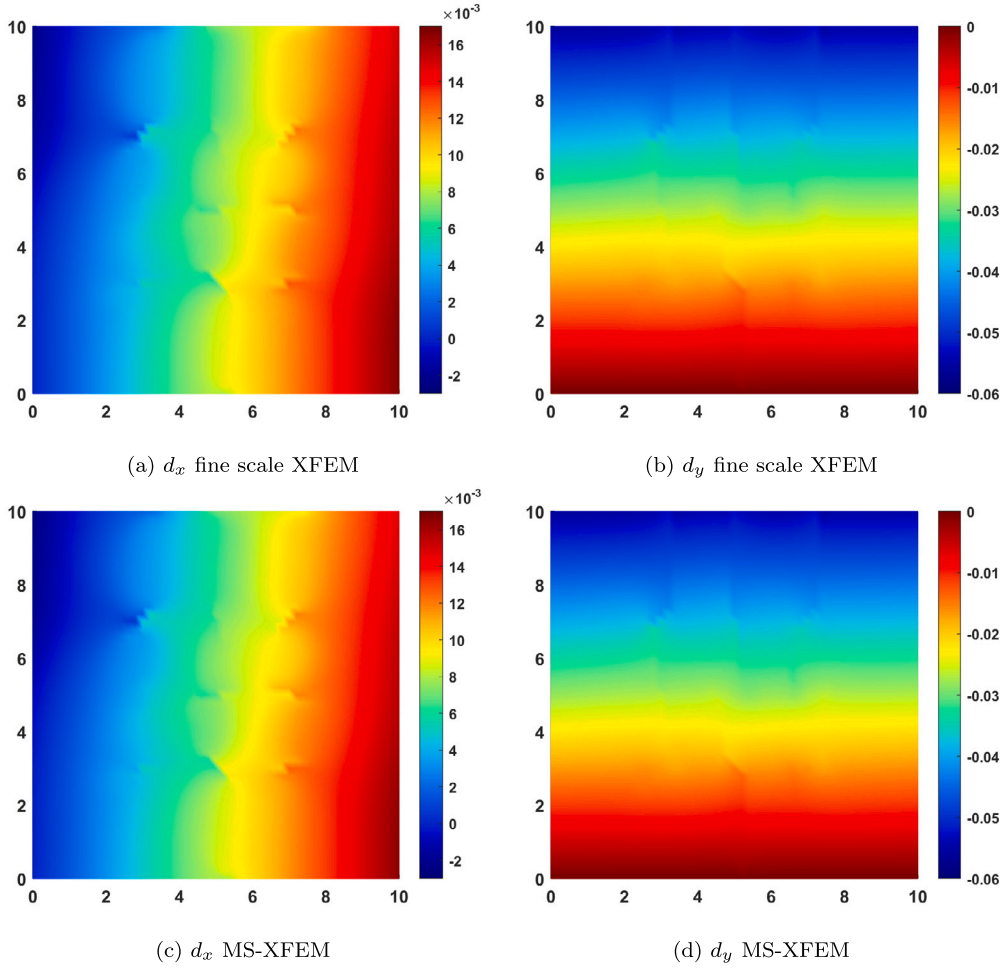

Fig. 26. Test case 4: Displacements fields simulated from fine scale XFEM and MS-XFEM with preconditioned GMRES using a tolerance of 10^{-2}.

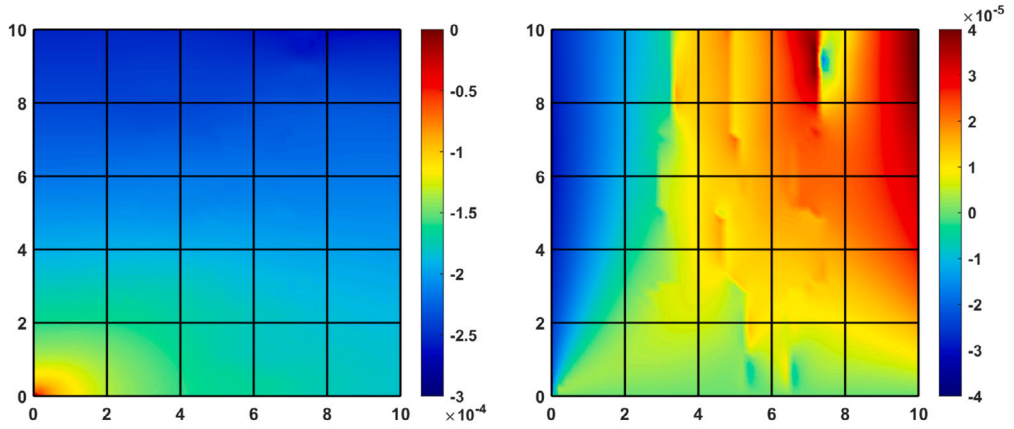

(a) error in d_x (b) error in d_y

Fig. 27. Test case 4: Displacement errors between simulations from fine-scale XFEM and MS-XFEM in the (a) x direction and (b) y direction. Black lines depict the coarse-scale mesh.

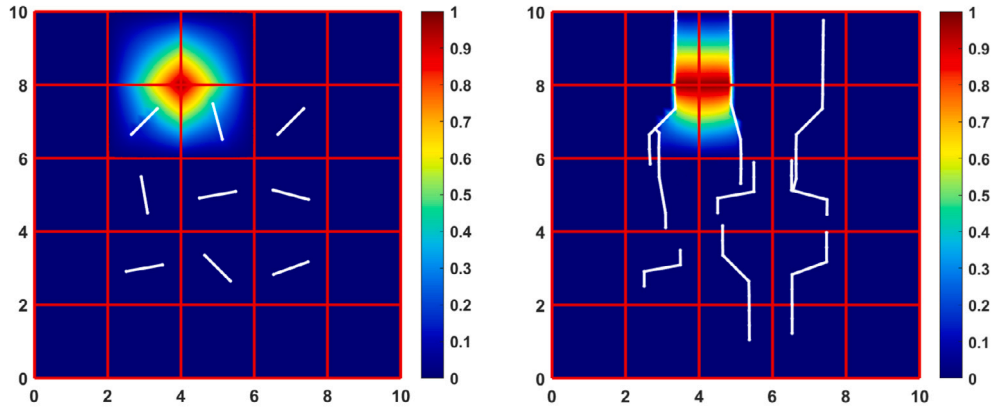

(a) P_{yy} at step 1 (b) P_{yy} at step 11

Fig. 28. Test case 4: Basis functions centered at the coarse mesh point $[4, 8]$ at time steps (a) 1 and (b) 11. Red lines represent the coarse mesh and white segments represent fractures.

the second test case, which demonstrates that wing crack paths simulated by MS-XFEM closely align with experimental observations. Subsequent cases further highlight MS-XFEM's capability in simulating the deformation of complex fracture networks and multiple fractures propagation within geological formations. All these results, along with the efficiency analysis of MS-XFEM in [48], emphasize MS-XFEM's significant potential for real-world applications in studying highly fractured geological formations, where precise and efficient modeling is crucial.

CRediT authorship contribution statement

Fanxiang Xu: Writing – original draft, Project administration, Methodology, Conceptualization. **Hadi Hajibeygi:** Writing – review & editing, Supervision, Resources. **Lambertus J. Sluys:** Writing – review & editing, Supervision, Resources.

Declaration of competing interest

The authors declare the following financial interests/personal relationships which may be considered as potential competing interests: Fanxiang Xu reports financial support was provided by China Scholarship Council. If there are other authors, they declare that they have no known competing financial interests or personal relationships that could have appeared to influence the work reported in this paper.

Acknowledgements

Fanxiang Xu acknowledges support from the China Scholarship Council (CSC, grant number 201807720039). The authors extend their gratitude to all members of the Delft Advanced Reservoir Simulation (DARSim) group, ADMIRE research group, and Computational Mechanics group in the Faculty of Civil Engineering and Geosciences at Delft University of Technology for their contributions and support.

Appendix A. Algorithm of fine-scale XFEM simulation strategy

Algorithm 1 Fine-scale XFEM simulation of fractures deformation.

Construct $\boldsymbol{K}^h$
Construct $\boldsymbol{K}_{con}$ following the "stick" state as Eq. (39)
while $\frac{\|\boldsymbol{r}^{i+1}\|}{\|\boldsymbol{r}_0\|} \geqslant \tau_r$ or $\frac{\|\Delta \boldsymbol{d}^{i+1}\|}{\|\boldsymbol{d}^i\|} \geqslant \tau_d$ **do**
  Update $(\boldsymbol{K}^p)^i = \boldsymbol{K}^h + (\boldsymbol{K}_{con})^i$
  Solve for the updated solution displacement $\Delta \boldsymbol{d}^{i+1}$
  Update $\boldsymbol{d}^{i+1} = \boldsymbol{d}^i + \Delta \boldsymbol{d}^{i+1}$
  Update $\boldsymbol{r}^{i+1}$ following Eq. (41)
  Update stick and slip conditions
  Update $\boldsymbol{K}_{con}^{i+1}$
end while

Algorithm 2 Fine-scale XFEM simulation of fracture propagation.

Construct $\boldsymbol{K}^h$
for $t = 1 \rightarrow$ final step **do**
  while $\frac{\|\boldsymbol{r}^{i+1}\|}{\|\boldsymbol{r}_0\|} \geqslant \tau_r$ or $\frac{\|\Delta \boldsymbol{d}^{i+1}\|}{\|\boldsymbol{d}^i\|} \geqslant \tau_d$ **do**
    check normal gap g_N at each Gauss point along the fractures
    if $g_N < 0$ **then**
      Construct $\boldsymbol{K}_{con}$ following the "stick" state as Eq. (39)
    else
      Construct $\boldsymbol{K}_{con}$ with all zero inputs
    end if
    Update $(\boldsymbol{K}^p)^i = \boldsymbol{K}^h + (\boldsymbol{K}_{con})^i$
    Solve for the updated solution displacement $\Delta \boldsymbol{d}^{i+1}$
    Update $\boldsymbol{d}^{h,i+1} = \boldsymbol{d}^{h,i} + \Delta \boldsymbol{d}^{h,i+1}$
    Update $\boldsymbol{r}^{h,i+1}$ following Eq. (41)
    Update stick and slip conditions
    Update $\boldsymbol{K}_{con}^{i+1}$
  end while
  Determine the group of fractures tips that will grow
  Update fractures geometries and level sets functions
  Update $\boldsymbol{K}^h$
end for

Appendix B. Algorithm of MS-XFEM simulation strategy

Algorithm 3 MS-XFEM simulation of fractures deformation.

Construct fine-scale $\boldsymbol{K}^h$ and basis functions $\boldsymbol{P}$
Construct $\boldsymbol{K}_{con}$ following the "stick" state as Eq. (39)
while $\frac{\|\boldsymbol{r}^{i+1}\|}{\|\boldsymbol{r}_0\|} \geqslant \tau_r$ or $\frac{\|\Delta \boldsymbol{d}^{i+1}\|}{\|\boldsymbol{d}^i\|} \geqslant \tau_d$ **do**
  Update $(\boldsymbol{K}^p)^i = \boldsymbol{K}^h + (\boldsymbol{K}_{con})^i$
  Construct $\boldsymbol{M}_{MS}^{-1}$ and $\boldsymbol{M}_{sm}^{-1}$
  Construct preconditioner $\boldsymbol{M}^{-1} = \boldsymbol{M}_{MS}^{-1} + \boldsymbol{M}_{sm}^{-1}(\boldsymbol{I} - (\boldsymbol{K}^p)^i \ \boldsymbol{M}_{MS}^{-1})$
  Solve for $\Delta \boldsymbol{d}^{h,i+1}$ with preconditioned GMRES following Eq. (59)
  Update $\boldsymbol{d}^{h,i+1} = \boldsymbol{d}^{h,i} + \Delta \boldsymbol{d}^{h,i+1}$
  Update $\boldsymbol{r}^{h,i+1}$ following Eq. (41)
  Update stick and slip conditions along Gauss points on the fracture
  Update $\boldsymbol{K}_{con}^{i+1}$
end while

Algorithm 4 MS-XFEM simulation of fracture propagation.

Construct fine-scale $\boldsymbol{K}^h$ and basis functions $\boldsymbol{P}$
for $t = 1 \rightarrow$ final step **do**
  while $\frac{\|\boldsymbol{r}^{i+1}\|}{\|\boldsymbol{r}_0\|} \geqslant \tau_r$ or $\frac{\|\Delta \boldsymbol{d}^{i+1}\|}{\|\boldsymbol{d}^i\|} \geqslant \tau_d$ **do**
    check normal gap g_N at each Gauss point along the fractures
    if $g_N < 0$ **then**
      Construct $\boldsymbol{K}_{con}$ following the "stick" state as Eq. (39)
    else
      Construct $\boldsymbol{K}_{con}$ with all zero inputs
    end if
    Update $(\boldsymbol{K}^p)^i = \boldsymbol{K}^h + (\boldsymbol{K}_{con})^i$
    Construct right preconditioner $\boldsymbol{M}^{-1}$
    Solve for $\Delta \boldsymbol{d}^{h,i+1}$ with preconditioned GMRES following Eq. (59)
    Update $\boldsymbol{d}^{h,i+1} = \boldsymbol{d}^{h,i} + \Delta \boldsymbol{d}^{h,i+1}$
    Update $\boldsymbol{r}^{h,i+1}$ following Eq. (41)
    Update stick and slip conditions along the fracture
    Update $\boldsymbol{K}_{con}^{i+1}$
  end while
  Determine the group of fractures tips that will grow
  Update fractures geometries and level sets functions
  Update $\boldsymbol{K}^h$
end for

Appendix C. Fracture coordinates of test case 3 and 4

Table C.5
Test case 3: Fracture coordinates.

Fracture	Coordinates	Fracture	Coordinates
1	[7.76, 51.86] - [35.86, 11.73]	8	[20.38, 33.84] - [38.40, 46.50]
2	[31.43, 59.90] - [63.55, 14.02]	9	[27.34, 8.20] - [45.36, 20.82]
3	[29.63, 78.16] - [43.97, 57.69]	10	[40.78, 27.37] - [53.40, 9.35]
4	[29.96, 63.75] - [46.00, 75.00]	11	[41.52, 7.14] - [59.54, 19.76]
5	[46.83, 78.00] - [58.88, 60.80]	12	[51.32, 51.84] - [64.52, 35.50]
6	[46.42, 59.41] - [64.45, 72.03]	13	[54.00, 38.00] - [72.99, 49.10]
7	[17.18, 52.36] - [34.50, 26.50]		

Table C.6
Test case 4: Fracture coordinates.

Fracture	Coordinates	Fracture	Coordinates
1	[2.51, 2.91] - [3.49, 3.09]	6	[6.52, 5.13] - [7.48, 4.87]
2	[4.65, 3.35] - [5.35, 2.65]	7	[2.65, 6.65] - [3.35, 7.35]
3	[6.53, 2.83] - [7.47, 3.17]	8	[4.87, 7.48] - [5.13, 6.52]
4	[2.91, 5.49] - [3.09, 4.51]	9	[6.65, 6.65] - [7.35, 7.35]
5	[4.51, 4.91] - [5.49, 5.09]		

Data availability

No data was used for the research described in the article.

References

[1] L. Hashemi, M. Blunt, H. Hajibeygi, Pore-scale modelling and sensitivity analyses of hydrogen-brine multiphase flow in geological porous media, Sci. Rep. 11 (1) (2021) 8348.
[2] L. Hashemi, M. Boon, W. Glerum, R. Farajzadeh, H. Hajibeygi, A comparative study for h2–ch4 mixture wettability in sandstone porous rocks relevant to underground hydrogen storage, Adv. Water Resour. 163 (2022) 104165.
[3] M. Boon, H. Hajibeygi, Experimental characterization of h 2/water multiphase flow in heterogeneous sandstone rock at the core scale relevant for underground hydrogen storage (uhs), Sci. Rep. 12 (1) (2022) 14604.
[4] W. van Rooijen, L. Hashemi, M. Boon, R. Farajzadeh, H. Hajibeygi, Microfluidics-based analysis of dynamic contact angles relevant for underground hydrogen storage, Adv. Water Resour. 164 (2022) 104221.
[5] K.R. Kumar, H.T. Honorio, H. Hajibeygi, Simulation of the inelastic deformation of porous reservoirs under cyclic loading relevant for underground hydrogen storage, Sci. Rep. 12 (1) (2022) 21404.
[6] Y. Wang, C. Vuik, H. Hajibeygi, Co2 storage in deep saline aquifers: impacts of fractures on hydrodynamic trapping, Int. J. Greenh. Gas Control 113 (2022) 103552.
[7] M. Zhao, Y. Wang, M. Gerritsma, H. Hajibeygi, Efficient simulation of co2 migration dynamics in deep saline aquifers using a multi-task deep learning technique with consistency, Adv. Water Resour. (2023) 104494.

[8] Z. Zhang, Y. Wang, C. Vuik, H. Hajibeygi, An efficient simulation approach for long-term assessment of CO2 storage in complex geological formations, in: SPE Reservoir Characterisation and Simulation Conference and Exhibition, OnePetro, 2023.
[9] S. Krevor, H. De Coninck, S.E. Gasda, N.S. Ghaleigh, V. de Gooyert, H. Hajibeygi, R. Juanes, J. Neufeld, J.J. Roberts, F. Swennenhuis, Subsurface carbon dioxide and hydrogen storage for a sustainable energy future, Nature Rev. Earth Environ. 4 (2) (2023) 102–118.
[10] T. Belytschko, Y.Y. Lu, L. Gu, Element-free Galerkin methods, Int. J. Numer. Methods Eng. 37 (Jan. 1994) 229–256.
[11] T. Belytschko, T. Black, Elastic crack growth in finite elements with minimal remeshing, Int. J. Numer. Methods Eng. 45 (5) (1999) 601–620.
[12] N. Moes, J. Dolbow, T. Belytschko, A finite element method for crack growth without remeshing, Int. J. Numer. Methods Eng. 46 (Sep. 1999) 131–150.
[13] A.R. Khoei, M. Vahab, E. Haghighat, S. Moallemi, A mesh-independent finite element formulation for modeling crack growth in saturated porous media based on an enriched-FEM technique, Int. J. Fract. 188 (Jun. 2014) 79–108.
[14] M. Rashid, The arbitrary local mesh replacement method: an alternative to remeshing for crack propagation analysis, Comput. Methods Appl. Mech. Eng. 154 (Feb. 1998) 133–150.
[15] T. Bittencourt, P. Wawrzynek, A. Ingraffea, J. Sousa, Quasi-automatic simulation of crack propagation for 2D lefm problems, Eng. Fract. Mech. 55 (09 1996) 321–334.
[16] J. Jiang, R.M. Younis, Hybrid coupled discrete-fracture/matrix and multicontinuum models for unconventional-reservoir simulation, SPE J. 21 (2016) 1009–1027.
[17] T.T. Garipov, P. Tomin, R. Rin, D.V. Voskov, H.A. Tchelepi, Unified thermo-compositional-mechanical framework for reservoir simulation, Comput. Geosci. 22 (4) (2018) 1039–1057.
[18] Y. Wang, M. Shahvali, Discrete fracture modeling using centroidal Voronoi grid for simulation of shale gas plays with coupled nonlinear physics, Fuel 163 (Jan. 2016) 65–73.
[19] A. Novikov, D. Voskov, M. Khait, H. Hajibeygi, J.D. Jansen, A scalable collocated finite volume scheme for simulation of induced fault slip, J. Comput. Phys. 469 (2022) 111598.
[20] H. Hajibeygi, D. Karvounis, P. Jenny, A hierarchical fracture model for the iterative multiscale finite volume method, J. Comput. Phys. 230 (2011) 8729–8743.
[21] Y. Efendiev, J. Galvis, G. Li, M. Presho, Generalized multiscale finite element methods. Oversampling strategies, Int. J. Multiscale Comput. Eng. 12 (6) (2014) 465–484.
[22] J.Y. Wu, F. Li, An improved stable XFEM (is-XFEM) with a novel enrichment function for the computational modeling of cohesive cracks, Comput. Methods Appl. Mech. Eng. 295 (Oct. 2015) 77–107.
[23] A.M. Aragón, A. Simone, The discontinuity-enriched finite element method, Int. J. Numer. Methods Eng. 112 (Sep. 2017) 1589–1613.
[24] F.P. Meer, L.J. Sluys, A phantom node formulation with mixed mode cohesive law for splitting in laminates, Int. J. Fract. 158 (May 2009) 107–124.
[25] K. Amir R, Extended Finite Element Method: Theory and Applications, John Wiley & Sons, Incorporated, 2015.
[26] C. Daux, N. Moës, J. Dolbow, N. Sukumar, T. Belytschko, Arbitrary branched and intersecting cracks with the extended finite element method, Int. J. Numer. Methods Eng. 48 (12) (2000) 1741–1760.
[27] S.S. Behbahani, H. Hajibeygi, D. Voskov, J.D. Jansen, Smoothed embedded finite-volume method (sefvm) for modeling contact mechanics in deformable faulted and fractured porous media, J. Comput. Phys. 459 (2022) 111143.
[28] L. Wang, C. Vuik, H. Hajibeygi, A stabilized mixed-Fe scheme for frictional contact and shear failure analyses in deformable fractured media, Eng. Fract. Mech. 267 (May 2022) 108427.
[29] J. Melenk, I. Babuška, The partition of unity finite element method: basic theory and applications, Comput. Methods Appl. Mech. Eng. 139 (1) (1996) 289–314.
[30] G. Allaire, Homogenization and two-scale convergence, SIAM J. Math. Anal. 23 (6) (1992) 1482–1518.
[31] A. Abdulle, E. Weinan, Finite difference heterogeneous multi-scale method for homogenization problems, J. Comput. Phys. 191 (1) (2003) 18–39.
[32] Y. Amanbek, G. Singh, M.F. Wheeler, H. van Duijn, Adaptive numerical homogenization for upscaling single phase flow and transport, J. Comput. Phys. 387 (2019) 117–133.
[33] K. Kumar, T. van Noorden, I.S. Pop, Upscaling of reactive flows in domains with moving oscillating boundaries, Discrete Contin. Dyn. Syst. 7 (2014) 623–644.
[34] H.-W. Zhang, J.-K. Wu, J. Lü, Z.-D. Fu, Extended multiscale finite element method for mechanical analysis of heterogeneous materials, Acta Mech. Sin. 26 (Dec. 2010) 899–920.
[35] R. Patil, B. Mishra, I. Singh, A new multiscale XFEM for the elastic properties evaluation of heterogeneous materials, Int. J. Mech. Sci. 122 (Mar 2017) 277–287.
[36] A. Khoei, M. Hajiabadi, Fully coupled hydromechanical multiscale model with microdynamic effects, Int. J. Numer. Methods Eng. 115 (Apr. 2018) 293–327.
[37] M.R. Hajiabadi, A.R. Khoei, A bridge between dual porosity and multiscale models of heterogeneous deformable porous media, Int. J. Numer. Anal. Methods Geomech. 43 (Oct. 2018) 212–238.
[38] H. Hajibeygi, P. Jenny, Multiscale finite-volume method for parabolic problems arising from compressible multiphase flow in porous media, J. Comput. Phys. 228 (Aug. 2009) 5129–5147.
[39] N. Castelletto, H. Hajibeygi, H.A. Tchelepi, Multiscale finite-element method for linear elastic geomechanics, J. Comput. Phys. 331 (Feb. 2017) 337–356.
[40] I. Sokolova, M.G. Bastisya, H. Hajibeygi, Multiscale finite volume method for finite-volume-based simulation of poroelasticity, J. Comput. Phys. 379 (Feb. 2019) 309–324.
[41] P. Jenny, S. Lee, H. Tchelepi, Multi-scale finite-volume method for elliptic problems in subsurface flow simulation, J. Comput. Phys. 187 (May 2003) 47–67.
[42] R. Deb, P. Jenny, Finite volume-based modeling of flow-induced shear failure along fracture manifolds, Int. J. Numer. Anal. Methods Geomech. 41 (Jul. 2017) 1922–1942.
[43] N. Castelletto, H. Hajibeygi, H. Tchelepi, Hybrid multiscale formulation for coupled flow and geomechanics, in: ECMOR XV - 15th European Conference on the Mathematics of Oil Recovery, EAGE Publications BV, Aug. 2016.
[44] B. Giovanardi, L. Formaggia, A. Scotti, P. Zunino, Unfitted FEM for modelling the interaction of multiple fractures in a poroelastic medium, in: Lecture Notes in Computational Science and Engineering, Springer International Publishing, 2017, pp. 331–352.
[45] H. Hajibeygi, G. Bonfigli, M.A. Hesse, P. Jenny, Iterative multiscale finite-volume method, J. Comput. Phys. 227 (Oct. 2008) 8604–8621.
[46] Y. Wang, H. Hajibeygi, H.A. Tchelepi, Algebraic multiscale solver for flow in heterogeneous porous media, J. Comput. Phys. 259 (2014) 284–303.
[47] E.T. Chung, Y. Efendiev, G. Li, An adaptive gmsfem for high-contrast flow problems, J. Comput. Phys. 273 (2014) 54–76.
[48] F. Xu, H. Hajibeygi, L.J. Sluys, Multiscale extended finite element method for deformable fractured porous media, J. Comput. Phys. 436 (Jul. 2021) 110287.
[49] F. Xu, H. Hajibeygi, L.J. Sluys, Adaptive multiscale extended finite element method (ms-xfem) for the simulation of multiple fractures propagation in geological formations, J. Comput. Phys. 486 (2023) 112114.
[50] F. Liu, R.I. Borja, A contact algorithm for frictional crack propagation with the extended finite element method, Int. J. Numer. Methods Eng. 76 (10) (2008) 1489–1512.
[51] R.I. Borja, Assumed enhanced strain and the extended finite element methods: a unification of concepts, Comput. Methods Appl. Mech. Eng. 197 (33–40) (2008) 2789–2803.
[52] V. Boltyanski, H. Martini, V. Soltan, Geometric Methods and Optimization Problems, vol. 4, Springer Science & Business Media, 1998.
[53] R.D. Cook, et al., Concepts and Applications of Finite Element Analysis, John Wiley & Sons, 2007.
[54] G.N. Wells, L.J. Sluys, Three-dimensional embedded discontinuity model for brittle fracture, Int. J. Solids Struct. 38 (Feb. 2001) 897–913.
[55] G. Zi, T. Belytschko, New crack-tip elements for xfem and applications to cohesive cracks, Int. J. Numer. Methods Eng. 57 (15) (2003) 2221–2240.
[56] S. Osher, J.A. Sethian, Fronts propagating with curvature-dependent speed: algorithms based on Hamilton-Jacobi formulations, J. Comput. Phys. 79 (Nov. 1988) 12–49.

[57] M. Stolarska, D.L. Chopp, N. Moës, T. Belytschko, Modelling crack growth by level sets in the extended finite element method, Int. J. Numer. Methods Eng. 51 (Jul. 2001) 943–960.
[58] Y. Saad, M.H. Schultz, GMRES: a generalized minimal residual algorithm for solving nonsymmetric linear systems, SIAM J. Sci. Stat. Comput. 7 (3) (1986) 856–869.
[59] G. Zhang, M. Wang, X. Li, S. Yue, Z. Wen, S. Han, Micro- and macrocracking behaviors in granite and molded gypsum containing a single flaw, Constr. Build. Mater. 292 (Jul. 2021) 123452.
[60] F. Liu, R.I. Borja, Stabilized low-order finite elements for frictional contact with the extended finite element method, Comput. Methods Appl. Mech. Eng. 199 (Aug. 2010) 2456–2471.